Self-consistent approach for modeling coupled elastic and visco-plastic processes induced by dislocation and pressure solution

Tingting Xu[a], Chloé Arson[a,*]

[a]*Georgia Institute of Technology, School of Civil and Environmental Engineering*

Abstract

This paper pesents a self-consistent approach in which coupled non-linear time-dependent deformation mechanisms are estimated by an affine approximation and elastic and visco-plastic macroscopic properties are calculated for the most general form of anisotropy. Phase changes from crystal to pore are accounted for, via a grain breakage mechanism. As an example, we study dislocation and pressure solution, two non-linear deformation mechanisms common to a wide range of polycrystalline materials. To this date, the couplings between the two are not fully understood. We analyze the sensitivity of the behavior of halite polycrystals to stress, brine content, grain size and grain breakage. Results indicate that: Pressure solution yields mechanical healing only if grain breakage is ignored; Otherwise, pressure solution accelerates dislocation creep, which results in an abrupt increase of elastic and viscoplastic compliance components; Higher stress and/or higher brine content enhance the coupled effects of pressure solution and dislocation; Pressure solution is

*Corresponding author

Email address: chloe.arson@ce.gatech.edu (Chloé Arson)

delayed by the occurrence of larger grains and by the entrapment of fluid in isolated pores. An interesting feature of the model is the representation of the pore space, which allows distinguishing the deformation mechanisms of these isolated pores from those of the pores where precipitation occurs.
Keywords: self-consistent method, elasto-viscoplasticity, coupled mechanisms, affine approximation, dislocation, pressure solution, anisotropy

1. Introduction

Dislocation and pressure solution are common to a wide range of polycrystalline materials, especially rocks in humid environments (Ashby, 1972; Rutter, 1976; Lehner, 1990, 1995; Arson et al., 2012; Arson, 2020). Dislocation glide occurs because of differences in mass and electronic valence between the atoms of a crystal. For instance, halite is a Face-Centered Cubic crystal (FCC), which presents six planes of weakness along which sliding occurs, among which, only two give rise to independent sliding mechanisms (Pouya, 2000). Pressure solution is the result of crystal dissolution at grain contacts under high normal stress, ion diffusion to least stressed contacts or pores through fluid films, and precipitation at those least stressed contacts or pores (Raj and Ashby, 1971; Rutter, 1983; Gundersen et al., 2002). While dislocation occurs in the crystal lattice, pressure solution takes place along the grain boundaries. Several phenomenological models have been proposed to predict the time-dependent behavior of polycrystalline materials subjected to different deformation processes (Chan et al., 1996; Munson, 1997; Hunsche and Hampel, 1999; Olivella and Gens, 2002; Urai and Spiers, 2007). However, coupling several deformation mechanisms from the grain scale to the

polycrystal scale remains challenging.

In the past decades, relationships were established between the internal structure of polycrystals and their plastic deformation (Adams and Olson, 1998). On the one hand, full-field approaches enable prediction of the actual micromechanical fields that develop inside each crystal (or phase). Crystal plasticity - based finite element (FE) implementations have been extensively used to simulate the plastic deformation of polycrystalline materials (Musienko et al., 2007; Roters et al., 2010). It should be noted that the sophistication of the crystal plasticity - based FEM approach comes with a high computational cost, which limits the size of the microstructures that can be investigated. Alternative to FEM, Fast Fourier Transform (FFT) - based full-field methods were proposed to model heterogeneous polycrystals (Moulinec and Suquet, 1994, 1998; Michel et al., 2000). For the same spatial resolution, the FFT method has proven to be very efficient in comparison with the standard FEM (Lebensohn, 2001; Lebensohn et al., 2008, 2012; Rovinelli et al., 2020). On the other hand, extensions of the mean-field models based on Eshelby's homogenization method (Eshelby, 1957) have been used to estimate the effective properties of polycrystalline aggregates. Homogenization models can be readily implemented in a FEM without representing explicitly the geometry of each feature of the microstructure. Therefore, mean-field methods are attractive for large-scale simulations, which would require too much computational power with a full-field method, and for problems in which information on microstructure is limited. The present paper aims to provide a mean-field estimate of the elastic-viscoplastic behavior of porous polycrystals under coupled dislocation and pressure solution deformation mechanisms.

One of the most commonly used homogenization methods for prediction of polycrystalline mechanical behavior is the self-consistent scheme, which was originally proposed by Kröner (1958) for estimating the overall elastic parameters of a polycrystal. This approach assumes that ellipsoidal inclusions are embedded in an infinite Homogeneous Equivalent Medium (HEM) that has the effective properties of the overall composite. The average strain and stress fields of the HEM are considered as reference fields. The homogenized properties of the Representative Elementary Volume (REV) are calculated iteratively, since the HEM stiffness tensor is yet-unknown in the HEM/inclusion interaction equations. Kröner (1961) and Budiansky and Wu (1962) independently developed elasto-plastic self-consistent models which neglect the plastic interactions between the inclusion and the surrounding matrix. To account for these interactions, Hill (1965) proposed an incremental self-consistent model for elasto-plastic materials, which was then applied to elasto-plastic polycrystals by Hutchinson (1970). Later, Berveiller and Zaoui (1979) proposed an extension to the self-consistent scheme with an isotropic elasto-plastic interaction between the inclusion and the matrix. It is less general than Hill's but more explicit and easier to apply. Iwakuma and Nemat-Nasser (1984) extended Hill's incremental approach to study the large elasto-plastic deformation of polycrystals. Ju (1991) proposed a two-dimensional self-consistent micromechanical damage model for microcrack-weakened brittle solids based on thermodynamics. González and LLorca (2000) proposed an elasto-plastic approach to compute the mechanical behavior of two-phase materials, including the change in the volume fraction of each phase.

The self-consistent method was also applied to time-dependent deformation processes in polycrystals. Hutchinson (1976) extended Hill's model to visco-plastic materials by using tangent creep compliances instead of elasto-plastic ones. Lebensohn and Tomé (1993) developed a tangent formulation at inclusion level by performing a Taylor's expansion based on the local tangent model proposed by Molinari et al. (1987). Then, Lebensohn et al. (2004) extended the modeling approach to deal with compressible polycrystals, and also considered the presence of ellipsoidal voids inside polycrystals subjected to large strain deformation. Masson and Zaoui (1999) proposed a self-consistent approach, applicable to arbitrary linearized behaviors, by means of the so-called affine procedure. Later, Molinari (2002) extended the affine averaging scheme to both viscoplastic and elasto-viscoplastic materials. Dogri et al. (2010) then refined the affine method in order to improve predictions and computational efficiency. Mercier and Molinari (2009) proposed two different self-consistent methods for elasto-viscoplastic materials. One was based on a separate homogenization of elastic and plastic properties and the other one was based on the additive interaction equation proposed by Molinari et al. (1997). Furthermore, a numerical implementation of the self-consistent method based on the additive interaction equation of Molinari et al. (1997) was proposed by Wang et al. (2012). However, Jeong and Tomé (2019) noted that the particular implementation of Wang et al. (2012) could lead to numerical inconsistencies and convergence issues. Zecevic and Lebensohn (2020) found that the numerical issues encountered in the implementation of Wang et al. (2012) were due to an incorrect definition of concentration tensors. They provided a correction to the approach of Wang

et al. (2012) and also developed a robust non-incremental interaction equation.

In all the modeling approaches reviewed above, the tangent and secant moduli are assumed to be uniform inside a given phase, that is, only average fields and properties are calculated within each phase. Fluctuations of the stress and strain fields in each phase can be taken into account by adopting a variational approach, in which the use of both first and second moments of the strain field deliver rigorous bounds (Castañeda, 1991). Generalized secant moduli, determined by the first and second moment of the field variables over the phases, yield estimates that are exact to the second order (Castañeda, 2002a,b). Variational approaches based on the second moments of strain and stress have recently been extended to elastic-viscoplastic materials (Lahellec and Suquet, 2007a,b; Brassart et al., 2012; Lahellec and Suquet, 2013; Agoras et al., 2016). The purpose of this study is to investigate coupled deformation mechanisms due to dislocation and pressure solution in polycrystals. Due to the complexity in considering the field fluctuations within phases for two time-dependent mechanisms, the self-consistent scheme is adopted in the present work.

In the proposed self-consistent approach, coupled non-linear time-dependent deformation mechanisms are estimated by an affine approximation, elastic and visco-plastic macroscopic properties are calculated through a closed form formulation that accounts for the most general form of anisotropy, and phase changes from single crystal to pore are accounted for, via a grain breakage mechanism. The polycrystal is represented by a HEM composed of three phases: single-crystals subject to dislocation and potential breakage, hol-

low sphere inclusions where pressure solution occurs, and isolated fluid-filled voids. The paper is organized as follows. Section 2 presents an extension of the non-incremental self-consistent homogenization method proposed by Zecevic and Lebensohn (2020) to include voids. Section 3 provides the microscopic constitutive relationships for dislocation and pressure solution deformation mechanisms, respectively. The resolution algorithm is described in Section 4. Section 5 summarizes some numerical applications of the model, where we take halite as a model material to study the influence of stress, brine content, grain size and grain breakage on the behavior of the polycrystal. Conclusions are drawn in Section 6.

In the following, we note vectors and second-order tensors with boldface letters, e.g., $\boldsymbol{n}$ denotes a normal vector, and $\boldsymbol{\epsilon}$, $\boldsymbol{\sigma}$ are the strain and stress tensors, respectively. Fourth-order tensors are noted with blackboard bold letters: e.g., $\mathbb{M}$ represents a compliance tensor. Time derivatives are noted with a dot superscript. Time derivatives are approximated by using the Euler backward method, as follows:

$$\dot{\boldsymbol{X}} = \frac{\boldsymbol{X}^{(t+\Delta t)} - \boldsymbol{X}^{(t)}}{\Delta t} \tag{1}$$

in which the superscript t denotes a value taken at the beginning of the current time step, while $t + \Delta t$ denotes a value taken at the end of the current time step. We adopt Cartesian notations and we use the convention of summation on the repeated indices (Einstein's notation). Tensor algebraic

operations are defined as follows (where := stands for "equivalent to"):

$$\begin{aligned} \text{Dot product} &: \boldsymbol{\sigma} \cdot \boldsymbol{n} := \sigma_{ij} n_j \\ \text{Double-dot product} &: \mathbb{M} : \boldsymbol{\sigma} := M_{ijkl}\sigma_{lk},\ \mathbb{P} : \mathbb{C} := P_{ijkl} C_{lkmn} \\ \text{Dyad} &: \boldsymbol{m} \otimes \boldsymbol{n} := m_i n_j \end{aligned} \tag{2}$$

2. Self-consistent modeling approach

In this section, we extend the non-incremental self-consistent homogenization method proposed by Zecevic and Lebensohn (2020) to include voids.

2.1. Eshelby's equivalent inclusion concept

Eshelby's homogenization method is based on a powerful concept called "eigenstrain", which is a generic name for inelastic strains such as thermal expansion, phase transformation, initial strain, plastic strain, and misfit strain (Mura, 1987). Consider a homogeneous material that occupies a domain D. When an eigenstrain is prescribed in a finite subdomain Ω, and when that eigenstrain is zero in the domain D-Ω, then Ω is called an inclusion, and D-Ω is called the matrix. Notice that both the inclusion and the matrix have the same elastic stiffness tensor. Eshelby (1957) showed that if the matrix is homogeneous, linearly elastic and infinitely extended, and if the inclusions are ellipsoidal, then the stress and strain fields in each inclusion are uniform. Let us denote the applied stress at infinity by $\boldsymbol{\Sigma}^0$ and the corresponding strain by $\boldsymbol{E}^0$. The so-called Eshelby tensor $\mathbb{S}$ relates the eigenstrain $\boldsymbol{\epsilon}^*$ to the inclusion strain field $\boldsymbol{\epsilon}$ when embedded in the matrix, as follows:

$$\boldsymbol{\epsilon} - \boldsymbol{E}^0 = \mathbb{S} : \boldsymbol{\epsilon}^* \tag{3}$$

For the most general case of macroscopic anisotropy, the Eshelby tensor is defined as the following surface integral over the unit sphere (Eshelby, 1957; Mura, 1987):

$$S_{ijkl} = \frac{1}{8\pi} C_{mnkl} \int_{-1}^{1} d\zeta_3 \int_{0}^{2\pi} (G_{imjn}(\bar{\zeta}) + G_{jmin}(\bar{\zeta})) d\omega \tag{4}$$

where

$$\begin{aligned} G_{ijkl}(\bar{\zeta}) &= \bar{\zeta}_k \bar{\zeta}_l N_{ij}(\bar{\zeta}) / D(\bar{\zeta}) \\ \bar{\zeta}_i &= \zeta_i / a_i;\ \zeta_1 = (1-\zeta_3^2)^{1/2} \cos\omega;\ \zeta_2 = (1-\zeta_3^2)^{1/2} \sin\omega;\ \zeta_3 = \zeta_3 \\ D(\bar{\zeta}) &= \epsilon_{mnl} K_{m1} K_{n2} K_{l3};\ N_{ij}(\bar{\zeta}) = \frac{1}{2} \epsilon_{ikl} \epsilon_{jmn} K_{km} K_{ln};\ K_{ik} = C_{ijkl} \bar{\zeta}_j \bar{\zeta}_l \end{aligned} \tag{5}$$

where a_1, a_2 and a_3 are the lengths of the semi-axes of the ellipsoidal inclusion, expressed in a rectangular Cartesian coordinate system. ϵ_{ijk} is the permutation tensor and C_{ijkl} is the matrix stiffness tensor. ω and ζ_3 are the angular position and the longitudinal coordinate, respectively. N_{ij} is the cofactor of K_{ij} and D is the determinant of K_{ij}. G is the second derivative of Green's function expressed in Fourier space.

If Ω is not subjected to any eigenstrain but has elastic properties that differ from those of the matrix, then Ω is called an inhomogenieity. If the inhomogeneity Ω is assigned an eigenstrain, then Ω is called an "inhomogeneous inclusion" and the macroscopic properties of the REV are calculated by means of the "equivalent inclusion" concept (Mura, 1987), by which the inhomogeneous inclusion with prescribed eigenstrain $\boldsymbol{\epsilon}^{*'}$ and elastic stiffness $\mathbb{C}'$ is replaced by an inclusion with an unknown eigenstrain $\boldsymbol{\epsilon}^{*}$ that is calculated by solving the following stress equivalence equation:

$$\boldsymbol{\sigma} = \mathbb{C}' : (\boldsymbol{\epsilon} - \boldsymbol{\epsilon}^{*'}) = \mathbb{C} : (\boldsymbol{\epsilon} - \boldsymbol{\epsilon}^{*}) \tag{6}$$

in which $\boldsymbol{\sigma}$ is the stress field in the inclusion and $\mathbb{C}$ is the stiffness tensor of the matrix.

As it will be explained in Section 3, we consider a porous polycrystalline REV made of solid and hollow spherical inhomogeneous inclusions. Pores are modeled as inhomogeneous inclusions with a zero stiffness and a pore pressure P_p. Eshelby's equivalent inclusion concept is used to reach a closed formulation of the self-consistent model.

2.2. Affine formulation

We approximate the local elasto-viscoplastic behavior of the equivalent inclusions by decomposing the local strain field ($\boldsymbol{\epsilon}_i$) into an elastic part ($\boldsymbol{\epsilon}_i^e$) and a viscoplastic part ($\boldsymbol{\epsilon}_i^{vp}$), and then resorting to an affine linearization (Masson et al., 2000):

$$\dot{\boldsymbol{\epsilon}}_i = \underbrace{\mathbb{M}_i^e : \dot{\boldsymbol{\sigma}}_i + \dot{\boldsymbol{\epsilon}}_i^{e0}}_{\dot{\boldsymbol{\epsilon}}_i^e} + \underbrace{\mathbb{M}_i^{vp} : \boldsymbol{\sigma}_i + \dot{\boldsymbol{\epsilon}}_i^{vp0}}_{\dot{\boldsymbol{\epsilon}}_i^{vp}} \tag{7}$$

in which the subscript "i" refers to the i^{th} inclusion type, and the superscripts "e" and "vp" denote the elastic component and viscoplastic component, respectively. The local stress $\boldsymbol{\sigma}_i$ and the local stress rate $\dot{\boldsymbol{\sigma}}_i$ are assumed to be uniform in the inclusion. $\mathbb{M}_i^e$ and $\mathbb{M}_i^{vp}$ are the elastic and viscoplastic compliance tensors, associated with the elastic prestrain rate $\dot{\boldsymbol{\epsilon}}_i^{e0}$ and viscoplastic prestrain rate $\dot{\boldsymbol{\epsilon}}_i^{vp0}$.

The macroscale field quantities are related to the microscale fields by volume average:

$$\begin{aligned} \boldsymbol{\Sigma} &= \frac{1}{V}\int_V \boldsymbol{\sigma} dV = \overline{\boldsymbol{\sigma}} \\ \boldsymbol{E} &= \frac{1}{V}\int_V \boldsymbol{\epsilon} dV = \overline{\boldsymbol{\epsilon}} \end{aligned} \tag{8}$$

where $\boldsymbol{\Sigma}$ and $\boldsymbol{E}$ are the macroscale stress and strain fields, respectively; V is the volume of the REV and $\overline{\bullet}$ denotes the volume average over the REV. Following a common assumption (Lebensohn et al., 2004; Mercier and Molinari, 2009), we consider that the HEM obeys affine relations analogous to Eq. 7:

$$\dot{\boldsymbol{E}} = \mathbb{M}^{e,hom} : \dot{\boldsymbol{\Sigma}} + \dot{\boldsymbol{E}}^{e0} + \mathbb{M}^{vp,hom} : \boldsymbol{\Sigma} + \dot{\boldsymbol{E}}^{vp0} \tag{9}$$

in which $\mathbb{M}^{e,hom}$ and $\mathbb{M}^{vp,hom}$ are the homogenized elastic and viscoplastic compliance tensors, respectively.

2.3. Self-consistent homogenization scheme

2.3.1. Interaction law

The problem of interaction between the elasto-viscoplastic inhomogeneous inclusions and the matrix in which these inclusions are embedded in is solved by using the Eshelby's equivalent inclusion concept (Eq. 6). The solution is similar to the elastic inclusion/matrix problem (Zecevic and Lebensohn, 2020):

$$\dot{\boldsymbol{\epsilon}}_i - \dot{\boldsymbol{\epsilon}}_i^* = \mathbb{M}^{e,hom} : \dot{\boldsymbol{\sigma}}_i + \dot{\boldsymbol{E}}^{e0} + \mathbb{M}^{vp,hom} : \boldsymbol{\sigma}_i + \dot{\boldsymbol{E}}^{vp0} \tag{10}$$

where $\dot{\boldsymbol{\epsilon}}_i^*$ is the eigenstrain rate of the equivalent inclusion. Applying Eq. 1, the non-incremental formulation can be expressed as:

$$\dot{\boldsymbol{\epsilon}}_i - \dot{\boldsymbol{\epsilon}}_i^* = \mathbb{M}^{e,hom} : \frac{\boldsymbol{\sigma}_i^{(t+\Delta t)} - \boldsymbol{\sigma}_i^{(t)}}{\Delta t} + \dot{\boldsymbol{E}}^{e0} + \mathbb{M}^{vp,hom} : \boldsymbol{\sigma}_i^{(t+\Delta t)} + \dot{\boldsymbol{E}}^{vp0} \tag{11}$$

For brevity, the superscript $t + \Delta t$ is ignored in the following. The above equation is thus noted:

$$\dot{\boldsymbol{\epsilon}}_i - \dot{\boldsymbol{\epsilon}}_i^* = \underbrace{(\frac{1}{\Delta t}\mathbb{M}^{e,hom} + \mathbb{M}^{vp,hom})}_{\mathbb{M}^{evp,hom}} : \boldsymbol{\sigma}_i \underbrace{- \frac{1}{\Delta t}\mathbb{M}^{e,hom} : \boldsymbol{\sigma}_i^{(t)} + \dot{\boldsymbol{E}}^{e0} + \dot{\boldsymbol{E}}^{vp0}}_{\dot{\boldsymbol{E}}^{evp0}} \tag{12}$$

According to Eshelby's theory, the eigenstrain rate $\dot{\boldsymbol{\epsilon}}_i^*$ is proportional to the difference between the local ($\dot{\boldsymbol{\epsilon}}_i$) and macroscopic ($\dot{\boldsymbol{E}}$) strain rate fields, as follows:

$$\dot{\boldsymbol{\epsilon}}_i - \dot{\boldsymbol{E}} = \mathbb{S}^{evp} : \dot{\boldsymbol{\epsilon}}_i^* \tag{13}$$

in which the elasto-viscoplastic Eshelby tensor $\mathbb{S}^{evp}$ can be calculated by replacing $\mathbb{C}$ by $(\mathbb{M}^{evp,hom})^{-1}$ in Eq. 4. Analytical expressions of the Eshelby tensor can only be obtained when the matrix is isotropic (Clyne and Withers, 1995) or transversely isotropic (Laws and McLaughlin, 1979). In the present study, in which the porous polycrystal may exhibit the most general form of anisotropy, the Eshelby tensor is estimated by using a Gauss-Legendre quadrature formula (Gavazzi and Lagoudas, 1990).

The non-incremental interaction law is then calculated as (Zecevic and Lebensohn, 2020):

$$\dot{\boldsymbol{\epsilon}}_i - \dot{\boldsymbol{E}} = -\widetilde{\mathbb{M}}^{evp} : (\boldsymbol{\sigma}_i - \boldsymbol{\Sigma}) + \frac{1}{\Delta t}\widetilde{\mathbb{M}}^{e} : (\boldsymbol{\sigma}_i^{(t)} - \boldsymbol{\Sigma}^{(t)}) \tag{14}$$

in which the interaction tensors are expressed as:

$$\begin{aligned} \widetilde{\mathbb{M}}_i^{evp} &= (\mathbb{I} - \mathbb{S}_i^{evp})^{-1} : \mathbb{S}_i^{evp} : \mathbb{M}^{evp,hom} \\ \widetilde{\mathbb{M}}_i^{e} &= (\mathbb{I} - \mathbb{S}_i^{evp})^{-1} : \mathbb{S}_i^{evp} : \mathbb{M}^{e,hom} \end{aligned} \tag{15}$$

The elasto-viscoplastic stress localization equation is similar to the purely viscoplastic one (Lebensohn et al., 2004):

$$\boldsymbol{\sigma}_i = \mathbb{B}^{evp} : \boldsymbol{\Sigma} + \boldsymbol{\Phi}_i \tag{16}$$

in which the localization tensors are defined as:

$$\begin{aligned} \mathbb{B}_i^{evp} &= (\mathbb{M}_i^{evp} + \widetilde{\mathbb{M}}^{evp}) : (\mathbb{M}^{evp,hom} + \widetilde{\mathbb{M}}^{evp}) \\ \boldsymbol{\Phi}_i &= (\mathbb{M}_i^{evp} + \widetilde{\mathbb{M}}^{evp}) : [\dot{\boldsymbol{E}}^{evp0} - \dot{\boldsymbol{\epsilon}}^{evp0} - \frac{1}{\Delta t}\widetilde{\mathbb{M}}^{e} : (\boldsymbol{\Sigma}^{(t)} - \boldsymbol{\sigma}_i^{(t)})] \end{aligned} \tag{17}$$

Pore equivalent inclusions, in which $\mathbf{\Phi} = (-P_p)\mathbf{I}$, where $\mathbf{I}$ is the second-order unit tensor, deform but cannot sustain any stress, i.e., $\mathbb{B}_{evp} = 0$. Strain concentration relations are thus needed to account for the inhomogeneity due to the pore equivalent inclusions on the strain distribution:

$$\dot{\boldsymbol{\epsilon}}_i = \mathbb{A}_i^{evp} : \dot{\boldsymbol{E}} + \mathbf{\Omega}_i \tag{18}$$

with

$$\begin{aligned}
&\mathbb{A}_i^{evp} = (\mathbb{C}_i^{evp} + \widetilde{\mathbb{C}}_i^{evp})^{-1} : (\mathbb{C}^{evp,hom} + \widetilde{\mathbb{C}}_i^{evp}) \\
&\mathbf{\Omega}_i = (\mathbb{C}_i^{evp} + \widetilde{\mathbb{C}}_i^{evp})^{-1} : [\mathbb{C}_i^{evp} : \dot{\boldsymbol{\epsilon}}_i^{evp0} - \mathbb{C}^{evp,hom} : \dot{\boldsymbol{E}}^{evp0} + \frac{1}{\Delta t}\widetilde{\mathbb{C}}_i^{e} : (\widetilde{\mathbb{C}}_i^{evp})^{-1} : (\boldsymbol{\sigma}^{(t)} - \mathbf{\Sigma}^{(t)})]
\end{aligned} \tag{19}$$

2.3.2. Homogenization method

The macroscopic stress and total strain field variables are equal to the volume average of the local stress and total strain field variables, which yields the following self-consistent effective properties:

$$\begin{aligned}
\mathbb{M}^{e,hom} &= \overline{\mathbb{M}_i^{e} : \mathbb{B}_i^{evp}} \\
\mathbb{M}^{evp,hom} &= \overline{\mathbb{M}_i^{evp} : \mathbb{B}_i^{evp}} \\
\dot{\boldsymbol{E}}^{evp0} &= \overline{\mathbb{M}_i^{evp} : \boldsymbol{\phi}_i + \dot{\boldsymbol{\epsilon}}_i^{evp0}}
\end{aligned} \tag{20}$$

In order to evaluate the average stress and strain fields in the pore equivalent inclusions, we use the following identities (Lebensohn et al., 2004):

$$\begin{aligned}
\mathbb{B}_i^{e/evp} : \mathbb{M}_i^{e/evp} &= \mathbb{A}_i^{e/evp} : \mathbb{M}_i^{e/evp,hom} \\
\mathbb{M}_i^{evp} : \boldsymbol{\phi}_i + \dot{\boldsymbol{\epsilon}}_i^{evp0} &= \mathbb{A}_i^{evp} : \dot{\boldsymbol{E}}_i^{evp0} + \mathbf{\Omega}_i
\end{aligned} \tag{21}$$

When inclusions have different shapes, they also have different Eshelby tensors, and in that case, the following self-consistent scheme should be used

(Walpole, 1969; Lebensohn et al., 2003, 2004):

$$\begin{aligned}
\mathbb{M}^{e,hom} &= \overline{\mathbb{M}_i^e : \mathbb{B}_i^{evp}} : \overline{\mathbb{B}_i^{evp}}^{-1} \\
\mathbb{M}^{evp,hom} &= \overline{\mathbb{M}_i^{evp} : \mathbb{B}_i^{evp}} : \overline{\mathbb{B}_i^{evp}}^{-1} \\
\dot{\boldsymbol{E}}^{evp0} &= \overline{\mathbb{M}_i^{evp} : \boldsymbol{\phi}_i + \dot{\boldsymbol{\epsilon}}^{evp0}}_i - \overline{\mathbb{M}_i^{evp} : \mathbb{B}_i^{evp}} : \overline{\mathbb{B}_i^{evp}}^{-1} : \overline{\boldsymbol{\Phi}_i}
\end{aligned} \tag{22}$$

In the following, we use Eq. 22 regardless of inclusion shapes, because that self-consistent scheme ensures numerical robustness, stability and convergence (Lebensohn et al., 2004).

3. Local affine formulation for single inclusions

3.1. Microstructure model

Dislocation and pressure solution are common causes of creep in polycrystals. In the following, we propose constitutive models to capture the coupled mechanisms that occur at the microscopic scale. We take halite as a model material to develop a closed formulation. Note however that the formulation is generalizable to any other polycrystalline material, porous or non porous, that is subjected dislocation glide and/or pressure solution.

In salt rock, dislocation glide originates crystal breakage, which accelerates the creep rate (Pouya et al., 2016). Crystal breakage is often referred to as grain breakage. In the following, we thus use single-crystal and grain interchangeably. Pressure solution, which can occur under similar stress and temperature conditions, triggers in-pore precipitation, which results in an increase of stiffness, also known as healing (Shen and Arson, 2019). To the authors' best knowledge, the micromechanical couplings between both phenomena and the resulting macroscopic behavior are not well understood.

To address this issue, we model a HEM that represents a porous polycrystal made of three phases: single crystals subject to dislocation glide, pressure solution inclusions, and isolated fluid-filled pores where pressure solution does not occur. Isolated pores represent fluid inclusions that may exist independently of the pores connected by a fluid film. For instance in halite, isolated brine pockets (Watanabe and Peach, 2002) and arrays of fluid inclusions were observed in the form of isolated spheres or tubes (Roedder, 1984; Ter Heege et al., 2005). Several spherical inclusion sets are defined for each phase: Single crystals are assigned various orientations; Pressure solution inclusions, which will be described in detail in Subsection 3.3, are assigned various orientations, grain sizes and initial porosities; Fluid-filled pores are assigned various volume fractions. We approximate the non-linear local behavior of each inclusion set by using an affine formulation. The macroscopic stiffness and compliance tensors of the HEM are calculated by solving the interaction laws stated in Eq. 14 for each inclusion set i. The resolution process is iterative, because the inclusions of each set are assumed to be embedded in the HEM of yet-unknown properties.

3.2. Single crystals subject to dislocation glide

The first set of inclusions represents the zones of influence single crystals subject to dislocation glide. Each gliding inclusion is spherical, and the elastic behavior of the single crystals is assumed to be linear and isotropic. The elastic compliance tensor of the single crystal inclusion is hereafter written as:

$$\mathbb{M}^e_{ijkl} = -\frac{\nu^s}{E^s}\delta_{ij}\delta_{kl} + \frac{1+\nu^s}{2E^s}(\delta_{ik}\delta_{jl} + \delta_{il}\delta_{jk}) \tag{23}$$

in which ν^s and E^s are the Poisson's ratio and the Young's modulus of solid (crystal). $\boldsymbol{\delta}$ is the Kronecker-delta.

The viscoplastic constitutive behavior of the single crystal is described by means of a non-linear rate-sensitive equation (non-Newtonian model):

$$\dot{\boldsymbol{\epsilon}}^{vp} = \sum_{l=1}^{L} \dot{\gamma}^l \boldsymbol{S}^l \tag{24}$$

in which $\dot{\gamma}^l$ denotes the viscoplastic slip rate corresponding to the l^{th} slip system. The symmetric part of the Schmid tensor $\boldsymbol{S}^l$ can be expressed as:

$$\boldsymbol{S}^l = \frac{1}{2}(\boldsymbol{n}^l \otimes \boldsymbol{m}^l + \boldsymbol{m}^l \otimes \boldsymbol{n}^l) \tag{25}$$

where $\boldsymbol{n}^l$ is the vector normal to the l^{th} slip plane and $\boldsymbol{m}^l$ is the l^{th} unit slip vector. The Schmid resolved shear stress for each slip system can be expressed as:

$$\tau^l = \boldsymbol{\sigma} : \boldsymbol{S}^l \tag{26}$$

For most crystals, the slip rate $\dot{\gamma}^l$ can be expressed as a power law of stress (Asaro, 1983). For example, laboratory experiments (Munson, 1997; Wawersik and Zeuch, 1986) showed that for halite:

$$\dot{\gamma}^l = C_0 \exp\left(-\frac{Q}{RT}\right)\left(\frac{|\tau^l|}{\tau_c^l}\right)^n \text{sign}(\tau^l) \tag{27}$$

where Q is the effective activation energy, R is the universal gas constant, T is the temperature, and τ_c^l is the critical resolved shear stress. The constants C_0 and n are constitutive parameters that require calibration.

For non-Newtonian viscous materials, the viscous stiffness and compliance tensors are no longer material constant quantities, as can be inferred from

the above equation. They depend on stress and on the strain rate. Following Hutchinson (1976), Eq. 24 can be written in a pseudo-linear form:

$$\dot{\boldsymbol{\epsilon}}^{vp} = \left\{ C_0 \exp\left(-\frac{Q}{RT}\right) \sum_{l}^{L} \frac{|\tau^l|^{n-1}}{(\tau_c^l)^n} \boldsymbol{S} \otimes \boldsymbol{S} \right\} : \boldsymbol{\sigma} = \mathbb{M}^{vp,(\mathrm{sec})} : \boldsymbol{\sigma} \tag{28}$$

where the superscript "sec" stands for secant. The secant scheme is known to yield overly stiff stress/strain responses. To alleviate this limitation, we apply a tangent linearization (Lebensohn and Tomé, 1993), as follows:

$$\dot{\boldsymbol{\epsilon}}^{vp} = \mathbb{M}^{vp,(\mathrm{tan})} : \boldsymbol{\sigma} + \dot{\boldsymbol{\epsilon}}^{vp0} \tag{29}$$

where the tangent and secant moduli fulfill the following relationship:

$$\mathbb{M}^{vp,(\mathrm{tan})} = n\mathbb{M}^{vp,(\mathrm{sec})} \tag{30}$$

in which the superscript "tan" stands for tangent and n is a real number. The back-extrapolated term can be expressed as:

$$\dot{\boldsymbol{\epsilon}}^{vp0} = (1-n)\dot{\boldsymbol{\epsilon}}^{vp} = (1-n)\mathbb{M}^{vp,(\mathrm{sec})} : \boldsymbol{\sigma} \tag{31}$$

It is noted that the single crystal is incompressible and therefore the constitutive relations can only be formulated in terms of the deviatoric part of the stress tensor, which implies that $\mathbb{M}^{vp}$ is invertible when defined as a 5 dimensional matrix. However in this study, the viscoplastic deformation induced by pressure solution is expressed in a 6-dimension space. To ensure that $\mathbb{M}^{vp}$ has a consistent dimension, some pre-processing is thus needed. Lebensohn et al. (1998) defined an Eshelby tensor that satisfies $S^{vp}_{ii11} + S^{vp}_{ii22} + S^{vp}_{ii33} = 0$ to ensure incompressibility. Alternatively, Hutchinson (1976) proposed a penalty method, which consists in adding a negligibly small compressibility to the

viscoplastic compliance matrix, thus allowing inversion of the compliance matrix in a 6-dimension space. In this study, we extended the 5-dimensional compliance matrix by using this penalty method. Let $\mathbf{M}$ be the Voigt notation of the compliance tensor $\mathbb{M}$. It was proven that a volumetric compliance less than $10^{-5}\mathbf{tr}(\mathbf{M})$ ensures invertibility of the viscoplastic compliance tensor with negligible influence on the constitutive predictions (Lebensohn and Tomé, 1993).

3.3. Pressure solution inclusions

The second set of inclusions represents zones influenced by pressure solution. The spherical inclusion model adopted in this study is similar to that initially proposed by Shen and Arson (2019). The pressure solution inclusion is a hollow sphere that is split by three orthogonal planes (see Fig. 1). These planes can be thought of as grain contact planes filled with a fluid film. The so-called "viscous film model" is adopted in this work, i.e., contact between solid grains is sustained by intergranular films of structured water (Rutter, 1976; Shimizu, 1995). When a contact plane is under normal compression, the solid shell of the hollow sphere dissolves on that plane. Ions diffuse towards the central pore of the hollow sphere, through the fluid film. The ions then precipitate at the walls of the free pore. Originally, the stress field in the hollow sphere inclusion was assumed to be homogeneous (Shen and Arson, 2019). In the present study, the stress field in the solid shell of the hollow sphere is calculated based on the knowledge of the average stress and strain fields of the hollow sphere. By so doing, we calculate the HEM viscoplastic compliance tensor as a function of the hollow sphere stress and strain fields, as opposed to updating the HEM compliance tensor with the porosity of the

hollow spheres only. The method requires homogenizing the stress and strain fields of the hollow sphere inclusion, which itself is a composite. In section 3.3.1, the elastic properties of the hollow sphere inclusion are calculated by considering a central pore embedded in a finite matrix. In section 3.3.2, the viscoplastic behavior of the hollow sphere inclusion induced by pressure solution is presented. The details are provided below.

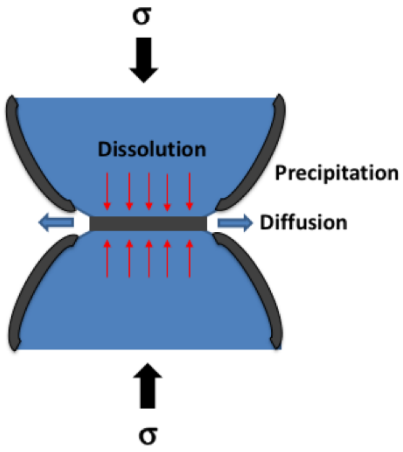

(a) Pressure solution mechanisms, adapted from (Yasuhara et al., 2003)

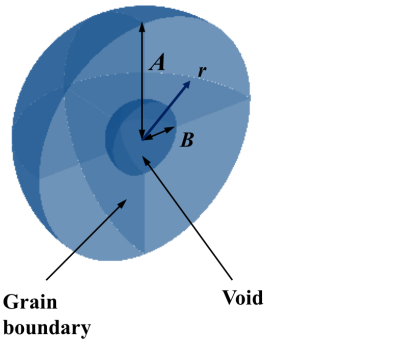

(b) Schematic representation of the hollow sphere inclusion, adapted from (Shen and Arson, 2019)

Figure 1: Hollow sphere inclusion subject to pressure solution

3.3.1. Mechanical behavior

To calculate the elastic properties of the hollow sphere inclusion, we consider the central pore as a homogeneous inclusion embedded in a finite solid domain (shell). The spherical pore inclusion has a radius B and is at the center of a finite spherical representative volume with radius A. The volume fraction of the pore is therefore $\phi = (B/A)^3$. For this problem of a spheri-

cal inclusion embedded in a finite spherical elastic matrix, Li et al. (2007a; 2007b) derived so-called "finite Eshelby tensors". They used Somigliana's identity and Green's function, which allowed them to extend the Mori-Tanaka method for a two-phased composite embedded in a finite REV. We adopt this method to model the hollow sphere inclusion. Let us define Ω^s and Ω^l the domains occupied by the solid phase and the fluid, respectively.

For the fluid-saturated pore, the local elastic problem can be posed as follows (Dormieux et al., 2006):

$$\boldsymbol{\sigma} = \mathbb{C} : \boldsymbol{\epsilon} + \boldsymbol{\sigma}^p \tag{32}$$

where $\mathbb{C}$ is a heterogeneous stiffness tensor, and $\boldsymbol{\sigma}^p$ is the pre-stress tensor:

$$\mathbb{C} = \begin{cases} 0 & (\Omega^l) \\ \mathbb{C}^s & (\Omega^s) \end{cases}, \quad \boldsymbol{\sigma}^p = \begin{cases} -P_l \mathbf{I} & (\Omega^l) \\ 0 & (\Omega^s) \end{cases} \tag{33}$$

in which the microscopic stress field in the pore is uniform and equal to $-P_l\mathbf{I}$. We consider that the solid shell is linear elastic, homogeneous and isotropic, and so the stiffness tensor $\mathbb{C}^s$ only depends on the bulk modulus K^s and on the shear modulus μ^s, i.e., $\mathbb{C}^s_{ijkl} = (3K^s - 2\mu^s)\delta_{ij}\delta_{kl}/3 + \mu^s(\delta_{ik}\delta_{jl} + \delta_{il}\delta_{jk})$.

The general finite Eshelby tensor is obtained by considering that the hollow sphere is subjected to a linear combination of prescribed displacement (Dirichlet) boundary conditions and prescribed traction (Neumann) boundary conditions (Li et al., 2007b; Sauer et al., 2008), as follows:

$$\mathbb{S}^{\bullet,F} = \alpha\mathbb{S}^{\bullet,D} + (1-\alpha)\mathbb{S}^{\bullet,N}, \quad \bullet = I, \text{or } E \tag{34}$$

where $\mathbb{S}^{\bullet,\star}$ is the finite Eshelby tensor. The first superscript $\bullet$ represents the interior solution for the pore ($\bullet = I$) or the exterior solution for the shell

($\bullet = E$), while the second superscript $\star$ stands for the general Eshelby tensor ($\star = F$), the Dirichlet-Eshelby tensor ($\star = D$) or the Neumann-Eshelby tensor ($\star = N$). The parameter α represents the fraction of the boundary subject to a Dirichlet boundary condition. The iterative resolution algorithm is initialized with an initial guess for the inclusion stress, which corresponds to a traction boundary condition ($\alpha = 0$).

The strain equation of state can be written as:

$$\boldsymbol{\epsilon}^{e,\mathrm{HS}} = (\mathbb{C}^{e,\mathrm{HS}})^{-1} : (\boldsymbol{\sigma}^{\mathrm{HS}} + P_l \boldsymbol{B}) \tag{35}$$

where:

$$\boldsymbol{B} = \phi \mathbf{I} : \mathbb{A}^p \tag{36}$$

in which it is reminded that ϕ is the volume fraction of the pore in the hollow sphere inclusion, and in which:

$$\mathbb{A}^p = [\mathbb{I} - (1-\phi)(< \mathbb{S}^{I,F} > - < \mathbb{S}^{E,F} >)]^{-1} \tag{37}$$

Using the finite Mori-Tanaka method, the homogenized elastic coefficients of the hollow sphere inclusion are the following:

$$\begin{aligned} K^{e,\mathrm{HS}} &= K^s - \phi K^s [1 - (1-\phi)\Delta s_1^F]^{-1} \\ \mu^{e,\mathrm{HS}} &= \mu^s - \phi \mu^s [1 - (1-\phi)\Delta s_2^F]^{-1} \end{aligned} \tag{38}$$

where $K^{e,\mathrm{HS}}$ and $\mu^{e,\mathrm{HS}}$ denote the effective bulk elastic modulus and shear elastic modulus of the hollow sphere inclusion, respectively. The expressions of the finite Eshelby tensors $\mathbb{S}^{\bullet,F}$ and the coefficients $\Delta s_i^F = s_i^{I,F} - s_i^{E,F}$ for $i = 1, 2$ are given in Appendix A. The estimated bulk modulus in Eq. 38 turns out to coincide with the bulk modulus in the infinite Mori-Tanaka solution (Mori and Tanaka, 1973; Dormieux et al., 2006), i.e., $K^{\mathrm{MT}} =$

$K^s \frac{4(1-\phi)\mu^s}{3\phi K^s+4\mu^s}$. For the shear modulus $\overline{\mu}$, the infinite Mori-Tanaka solution $\mu^{\mathrm{MT}} = \mu^s \frac{(1-\phi)(9K^s+8\mu^s)}{9K^s(1+\frac{2}{3}\phi)+8\mu^s(1+\frac{3}{2}\phi)}$ can be recovered as $\gamma_u \to 0$ and $\gamma_t \to 0$.

3.3.2. Chemical behavior

The viscoplastic constitutive model of the hollow sphere inclusion relates the rate of mechanical work to the rate of dissipation induced by grain boundary diffusion (Lehner, 1990; Shen and Arson, 2019). Several assumptions are made: (1) The hollow sphere inclusion is a "closed system", i.e., there is no long range exchange of solid mass and there is no fluid transport from or to the surroundings (Rutter, 1976; Spiers and Schutjens, 1990); (2) The characteristic sizes A and B are equal in all directions, i.e., the inclusion is indeed a hollow sphere; (3) In halite, pressure solution is diffusion controlled (Spiers and Schutjens, 1990); (4) Chemical potential differences are only induced by the normal stress, i.e., only the normal stress components contribute to the creep process; (5) Dissolving grain-to-grain contacts remain flat and thus the dissolution velocity is uniform over each grain contact area.

Mass conservation requires that, at steady state, the mass of ions transported by diffusions equals that of solid dissolved, so that,

$$J(r)A_p = \frac{2V_{ps}A_c}{\Omega} \tag{39}$$

in which $J(r)$ is the radial flux, Ω is the molar volume, $A_c = \pi(A^2 - r^2)$ is the contact surface area and V_{ps} is the uniform contact dissolution velocity. $A_p = 2\pi rS$ is the peripheral area at radius r that is open to the radial diffusive flux $J(r)$, where S denotes the mean thickness of fluid in the grain boundary zone (see Fig. 1).

Differentiating $\mu = \mu_0 + RT\ln(C/C_0)$ with respect to C, one obtains

$\partial\mu/\partial C = RT/C$, which, combined with Fick's law, yields:

$$J(r) = -D\frac{\partial C}{\partial r} = -\frac{DC(r)}{RT}\frac{\partial \mu}{\partial r} \tag{40}$$

where D is the grain boundary diffusion coefficient.

Neglecting grain boundary sliding (Rutter, 1976), the rate of dissipation at the grain contacts is set equal to the rate of dissipation due to the transfer of mass (Lehner, 1990; Shen and Arson, 2019):

$$d\dot{\Delta}_r = -J(r)A_p\frac{\partial \mu}{\partial r}dr \tag{41}$$

Assuming that, under low contact stress, $C(r)$ is uniform in the pore, i.e., $C(r) \approx C_0$, then the integral of Eq. 41 simplifies into:

$$\dot{\Delta}_r = \int_A^B \frac{2RTV_{ps}^2\pi(A^2 - r^2)^2}{DSC_0\Omega^2 r}dr \tag{42}$$

Moreover, the stress average condition gives:

$$\boldsymbol{\sigma}^{\mathrm{HS}} = \frac{1}{|\Omega_0|}\left[\int_{\Omega^s}\boldsymbol{\sigma}dV_z + \int_{\Omega^l}(-P_l\mathbf{I})dV_z\right] = (1-\phi)\boldsymbol{\sigma}^s - \phi P_l\mathbf{I} \tag{43}$$

in which the $\boldsymbol{\sigma}^s$ represents the stress field in the solid shell. Therefore, the mechanical work input rate along the i^{th} direction during viscoplastic deformation can be expressed as follows:

$$\dot{W}^i = 2A_cV_{ps}\boldsymbol{\sigma}^s \cdot \boldsymbol{n}_i \tag{44}$$

in which $\boldsymbol{n}_i$ represents the direction normal to the i^{th} contact plane in the hollow sphere ($i = 1, 2, 3$).

The mechanical work that causes deformation during diffusion controlled creep is fully dissipated by grain boundary diffusion (Pluymakers and Spiers,

2015; Spiers and Schutjens, 1990). So, we consider that the rate of increase of the Helmholtz energy of the solid phase and the changes in surface energy caused by island growth/contraction are negligible. The mechanical work input is thus entirely dissipated by pressure solution, which translates into:

$$\dot{W}^i = \dot{\Delta}^i_r \tag{45}$$

Note that the energy/entropy balance is considered along each direction independently.

Combing Eq. 42 with Eq. 45 yields the expression of the rate of volume change due to pressure solution in each direction i:

$$V^i_{ps} = \frac{DSC_0\Omega^2(A^2-B^2)}{RT\int_B^A \frac{(A^2-r^2)^2}{r}dr}\boldsymbol{\sigma}^s \cdot \boldsymbol{n}_i \tag{46}$$

Substituting Eq. 43 into the above equation yields the corresponding strain rate, as follows:

$$\dot{\boldsymbol{\epsilon}}^{ps} \cdot \boldsymbol{n}_i = \frac{V^i_{ps}}{A} = \underbrace{\frac{DSC_0\Omega^2(A^2-B^2)}{ART\int_B^A \frac{(A^2-r^2)^2}{r}dr}}_{\mathcal{G}}\boldsymbol{\sigma}^s \cdot \boldsymbol{n}_i = \mathcal{G}\frac{[\boldsymbol{\sigma}^{\mathrm{HS}} - \phi(-P_l\mathbf{I})]\cdot \boldsymbol{n}_i}{1-\phi} \tag{47}$$

where $\dot{\boldsymbol{\epsilon}}^{ps}$ is the viscoplastic strain due to pressure solution. We introduce the pressure solution compliance tensor $\mathbb{M}^{ps}$, defined as:

$$\dot{\boldsymbol{\epsilon}}^{ps} = \mathbb{M}^{ps} : [\boldsymbol{\sigma}^{\mathrm{HS}} - \phi(-P_l\mathbf{I})] \tag{48}$$

Since it is assumed that only normal stress components contribute to the creep deformation in the hollow sphere inclusion, we propose to only relate the normal stress to the normal pressure solution strain rate, as follows:

$$\mathbb{M}^{ps}_{1111} = \mathbb{M}^{ps}_{2222} = \mathbb{M}^{ps}_{3333} = \frac{\mathcal{G}}{(1-\phi)} \tag{49}$$

with the other components of the $\mathbb{M}^{ps}$ tensor being zero.

Taking the time derivative of Eq. 35, we get:

$$\dot{\boldsymbol{\epsilon}}^{e,\mathrm{HS}} = \mathbb{M}^{e,\mathrm{HS}} : (\dot{\boldsymbol{\sigma}}^{\mathrm{HS}} + P_l \dot{\boldsymbol{B}}) + \dot{\mathbb{M}}^{e,\mathrm{HS}} : (\boldsymbol{\sigma}^{\mathrm{HS}} + P_l \boldsymbol{B}) \tag{50}$$

in which $\mathbb{M}^{e,\mathrm{HS}} = (\mathbb{C}^{e,\mathrm{HS}})^{-1}$. The second term on the right-hand side arises because of the dependence of the elastic properties on the porosity of the inclusions, which decreases as precipitation occurs, hence resulting in so-called "mechanical healing" (Miao et al., 1995). Combining Eq. 47 and Eq. 50, we obtain:

$$\begin{aligned} \dot{\boldsymbol{\epsilon}}^{\mathrm{HS}} &= \mathbb{M}^{e,\mathrm{HS}} : (\dot{\boldsymbol{\sigma}}^{\mathrm{HS}} + P_l \dot{\boldsymbol{B}}) + \dot{\mathbb{M}}^{e,\mathrm{HS}} : (\boldsymbol{\sigma}^{\mathrm{HS}} + P_l \boldsymbol{B}) + \mathbb{M}^{ps} : (\boldsymbol{\sigma}^{\mathrm{HS}} - \phi(-P_l \mathbf{I})) \\ &= \mathbb{M}^{e,\mathrm{HS}} : \dot{\boldsymbol{\sigma}}^{\mathrm{HS}} + (\dot{\mathbb{M}}^{e,\mathrm{HS}} + \mathbb{M}^{ps}) : \boldsymbol{\sigma}^{\mathrm{HS}} + P_l \mathbb{M}^{e,\mathrm{HS}} : \dot{\boldsymbol{B}} + \mathbb{M}^{ps} : \phi(P_l \mathbf{I}) \end{aligned} \tag{51}$$

4. Numerical algorithm

In what follows, we explain the iterative procedure to calculate the micro and macro stress and strain fields in the proposed elasto-viscoplastic self-consistent model. In a typical boundary value problem, either the macroscopic stress rate $\dot{\boldsymbol{\Sigma}}$ or the macroscopic strain rate $\dot{\boldsymbol{E}}$ is a given function of time. The n^{th} step corresponds to time $t_n = n\Delta t$, Δt being the time increment. The subscript i and the superscript j stand for the i^{th} inclusion and the j^{th} iteration, respectively. In order to start an iterative algorithm to solve for the local stress and strain states, one should assume initial input values for the local stresses $\boldsymbol{\sigma}_i$. For the first deformation step, we take $\boldsymbol{\sigma}_i^0 = \dot{\boldsymbol{\Sigma}}$ in which $\boldsymbol{\Sigma}$ is the given far field stress, or, if the given far field is a strain, we

assume initially that the behavior is linear elastic and $\boldsymbol{\sigma}_i^0 = \mathbb{C}^e : \dot{\boldsymbol{E}}$. In the following steps, the stress of the previous step is the trial stress value in the inclusion. The self-consistent algorithm is composed of two nested iterative loops, as explained in Algorithm 1.

Algorithm 1: The double nested loop used in the algorithm.

$\boldsymbol{\sigma}_{i,n}^1 = \dot{\boldsymbol{\Sigma}}_n$ or $\boldsymbol{\sigma}_{i,n}^1 = \mathbb{C}^e : \dot{\boldsymbol{E}}_n$ for $n = 1$; $\boldsymbol{\sigma}_{i,n}^1 = \boldsymbol{\sigma}_{i,n-1}$ for $n > 1$;

`// Initialize the values for the local stresses`

while $|\boldsymbol{\sigma}_{i,n}^{j+1} - \boldsymbol{\sigma}_{i,n}^{j}| > tol$ **do**

  Calculate $\mathbb{M}_i^{e/evp}$ and $\boldsymbol{\epsilon}_i^{evp0}$ (Eq. 29 and Eq. 51) ; `// Calculate local linearized formulation for each inclusion`

  $\mathbb{M}_n^{e/evp,hom,1} = \overline{\mathbb{M}}_i^{e/evp}$, $\dot{\boldsymbol{E}}_n^{evp0,1} = \overline{\dot{\boldsymbol{\epsilon}}_i^{evp0}}$ for $n = 1$;
  $\mathbb{M}_n^{e/evp,hom,1} = \mathbb{M}_{n-1}^{e/evp,hom}$, $\dot{\boldsymbol{E}}_n^{evp0,1} = \dot{\boldsymbol{E}}_{n-1}^{evp0,1}$ for $n > 1$;
  `// Initialize the values for macroscopic compliance tensors`

  while $|\mathbb{M}_n^{e/evp,hom,j+1} - \mathbb{M}_n^{e/evp,hom,j}| > tol$ **do**

    Calculate $\mathbb{S}_i^{e,evp}$, $\mathbb{A}_i^{e,evp}$ and $\mathbb{B}_i^{e,evp}$ (Eq. 4, Eq. 15 and Eq. 17) ; `// Get Eshelby, interaction and concentration tensors`

    Update $\mathbb{M}_n^{e/evp,hom,j+1}$ (Eq. 20) ; `// Update the macroscopic compliance tensors`

  end

  Update $\boldsymbol{\sigma}_{i,n}^{j+1}$; `// Update the local stresses`

end

Within the innermost loop, the local elasto-viscoplastic compliance tensor $\mathbb{M}_i^{evp}$ and back-extrapolated term $\boldsymbol{\epsilon}_i^{evp0}$ are obtained for each inclusion. Next, the first estimates of the macroscopic compliance tensor $\mathbb{M}^{e/evp,hom}$ and of the back-extrapolated term $\boldsymbol{E}^{evp0}$ are calculated from the volume averages of the corresponding local quantities. In subsequent calculation steps, the values of $\mathbb{M}^{e/evp,hom}$ and $\boldsymbol{E}^{evp0}$ are derived from mircoscopic field variables calculated at the previous step. With that information on the HEM, the Eshelby tensors and interaction tensors can be calculated. Subsequently, the concentration tensors can be obtained as well. New (better) estimates of $\mathbb{M}^{e/evp,hom}$ and $\boldsymbol{E}^{evp0}$ are then obtained. The iteration is repeated until the convergence on these quantities is achieved, in which case the innermost procedure is terminated. The macroscopic stress or strain is therefore calculated through the constitutive relationship of the REV together with the far field stress or strain. Next, the local stresses are updated from the stress-dependent local viscoplastic compliance tensor $\mathbb{M}_i^{vp}$. If the recalculated $\boldsymbol{\sigma}_i$ coincides with the value assumed at the beginning of the innermost loop with a certain tolerance, $\dot{\boldsymbol{E}}$ or $\dot{\boldsymbol{\Sigma}}$ can be imposed at the next step. If the convergence conditions are not fulfilled, the recalculated $\boldsymbol{\sigma}_i$ is used as the new guess and the innermost iteration loop starts again. In the present implementation, the tolerances are all set to 0.01, after Lebensohn (1993).

5. Numerical results

Salt rock is a favorable host medium for geological storage of radioactive waste (Carter et al., 1993), petroleum (Zhang et al., 2017), natural gas

(Staudtmeister and Rokahr, 1997) and compressed air (Fan et al., 2019). A number of phenomenological models were proposed to predict salt rock deformation, but these approaches are not suitable for investigating the influence of microstructural attributes on strain rates (Carter et al., 1982; Senseny et al., 1992; Munson and Dawson, 1979). In this section, we take halite as an example material to illustrate the capabilities of the self-consistent elasto-viscoplastic model presented in Sections 2 and 3. In the following, f_{HS} and f_p denote the ratios of the hollow sphere pore volume and of the fluid-filled pore volume to the total pore volume in the REV, respectively. We have $f_{\mathrm{HS}} + f_p = 1$.

5.1. Model calibration and microstress evolution in dry conditions

Spiers et al. (1988) performed compaction creep experiments on dry and wet granular salt rock in oedometric conditions, under various stress levels. To study halite in dry conditions, the specimens were flushed with argon gas before being compacted at an effective pressure of 2MPa, thus producing a well-controlled starting aggregate with an initial porosity of $\phi_0 = 41 \pm 1\%$. The specimens were then loaded vertically at constant stress. We simulated the dry creep tests with an initial microstructure that consisted of 500 spherical single-crystal inclusions and 500 spherical pressure solution inclusions, with a uniform distribution of orientations (Jiang, 2007).

During the experiments, no evidence of pressure solution was found. For instance, no indentation or overgrowth was detected in the microscopic images taken at several stages of the dry creep tests (Spiers et al., 1988; Watanabe and Peach, 2002). Spiers et al. (1988) concluded that the compaction of dry (i.e., brine-free) specimens occurred because of a dislocation mechanism,

presumably with accommodation by particle sliding and minor microcracking. For that reason, we calibrated the dislocation glide parameters against volumetric strain vs. time curves obtained in dry conditions. Data obtained under a vertical stress of 6 MPa was used for calibration, and the experimental results obtained under 4.2 MPa and 8 MPa were used for verification. All the experiments were performed on specimens with a grain size of $d = 275\mu m$. To inactivate the pressure solution mechanism in the model, the pore volume fraction of the pressure solution inclusions was taken equal to zero, i.e., $f_p = 1$. The volume fraction of the fluid-filled pores (argon-filled in this case) was set equal to the initial porosity of the specimens under study. The calibrated parameters are reported in Table 1 and the results are shown in Fig. 2. The model captures the transition between primary creep (high deformation rate) and secondary creep (low deformation rate) after a few hours. The deformation measured after two days is predicted with excellent accuracy. As expected, the volumetric strain at a given time increases with stress.

In order to gain a deeper understanding of the deformation mechanisms that take place during the test, we plotted the distributions of microscopic principal stresses in the different sets of inclusions under an axial stress of 6 MPa (Fig. 3). For each inclusion, the principal values of the microstress can be represented by a vector $\overrightarrow{\sigma}$ with a radial coordinate (on the horizontal axis) and an axial coordinate (on the vertical axis). In the maps, markers represent the end points of the vectors. Tensile microstresses (respectively, compressive microstresses) are plotted in the top-right quadrant (respectively, in the bottom-left quadrant). Since all the creep tests are con-

Table 1: Elasto-viscoplastic self-consistent model parameters. Elasticity and dislocation parameters are calibrated against dry creep tests (Subsection 5.1). Pressure solution parameters are calibrated against wet creep tests (Subsection 5.2).

	Symbol	Definition	Values	Units
Elasticity	E	Young's modulus	25	GPa
	ν	Poisson's ratio	0.37	–
Dislocation	Q	Activation energy	5.8e7	mJ/mol
	C_0	Rate constant	1	–
	n	Stress exponent	8.6	–
	τ_c^l	Critical resolved shear stress	5	MPa
Pressure solution	DCS	Grain boundary diffusivity	1.24e-10	mm^2/s

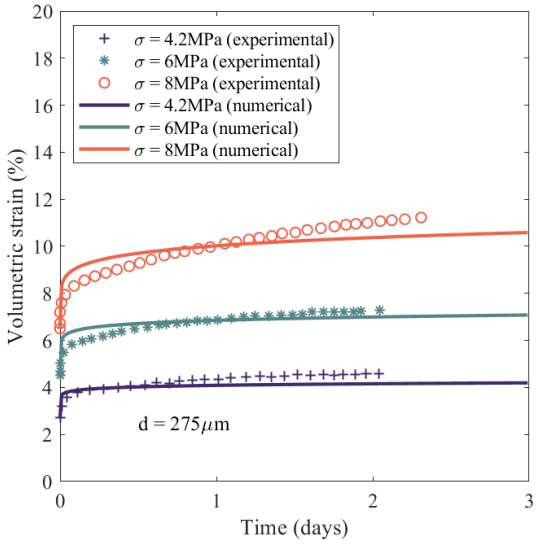

Figure 2: Comparison between numerical results and experimental data in dry conditions at various axial stresses.

ducted in oedometer conditions, i.e., with fixed radial (lateral) displacements, all the principal stresses are initially compressive. In dry conditions, the only deformation mechanism at stake is dislocation, thus the microstresses in the hollow sphere inclusions remain almost constant throughout the creep test. In the single crystal inclusions, the difference between major and minor principal stresses remains small. Since dislocation is controlled by the deviatoric stress, crystal inclusions do not undergo large deformation, which explains the low deformation rate observed macroscopically. Moreover, the principal stresses in single crystal inclusions rotate only slightly during the creep test and remain relatively stable over time, which translates into a plateau of the volumetric strain at the REV scale. As an example, the circles in Fig. 3 track the evolution of the state of stress in one of the 500 crystal inclusions, which is plotted against time in Fig. 4. Results show that from 0.1 days to 3 days, the rotation of the principal stresses is around 20 % while the magnitude change is about 2 %. In the experiments, an asymptotic deformation is reached after two days under 4.2 MPa and 6 MPa, but not under 8 MPa (Fig. 2). In the simulations, the volumetric strain reaches a plateau no later than two days under all stress levels. This can be explained by the absence of significant stress rotation and deviatoric stress in the single crystal inclusions under oedometric conditions, as shown in Fig. 3. Since the microstress state in the crystal inclusions is relatively stable over time, we observe a discrepancy of the order of 10% between the numerical and experimental results during the first few hours of the creep test under 8 MPa. The error becomes negligible after one day. Fig. 5 shows the evolution of elastic and viscoplastic compliance tensors, respectively. The largest eigenvalue of the viscoplastic

compliance tensor decreases abruptly in the first few hours, which is consistent with the sharp decrease in volumetric strain rate over that period of time. Overall, as could be expected from Eqs. 23 and 30, the changes in the elastic and viscoplastic compliance tensors are negligible when the specimen is solely subjected to dislocation glide. This is because the viscoplastic compliance tensor of the dislocation inclusions is stress-dependent. Hollow sphere inclusions do not interact significantly with the crystal inclusions, which are therefore subjected to a quasi-constant stress during the creep test.

5.2. Model calibration and microstress evolution in wet conditions

In the experiments conducted by Spiers' group to study halite in wet conditions, NaCl powder with initial porosity $\phi_0 = 42 \pm 3\%$ was dry-compacted and then unloaded and flooded with saturated brine at a temperature of 22° and at a pressure of 1 atm (Spiers et al., 1988). The pore brine was maintained at a pressure of 1 atm during the subsequent uniaxial creep test. Like for the dry tests, we simulated the wet creep tests with an initial microstructure that consisted of 500 spherical single-crystal inclusions and 500 spherical pressure solution inclusions, with a uniform distribution of orientations (Jiang, 2007).

In wet conditions, micrographs indicated the occurrence of grain-to-grain indentation, contact truncation, and grain shape changes. Overgrowths were also observed on pore walls. Spiers et al. (1988) concluded that the deformation of the wet specimens was dominated by a pressure solution mechanism. We thus simulated the wet creep tests by activating both the dislocation mechanism and the pressure solution mechanism. The volume fraction of the fluid-filled voids was taken equal to zero, i.e., $f_p = 0$. The volume frac-

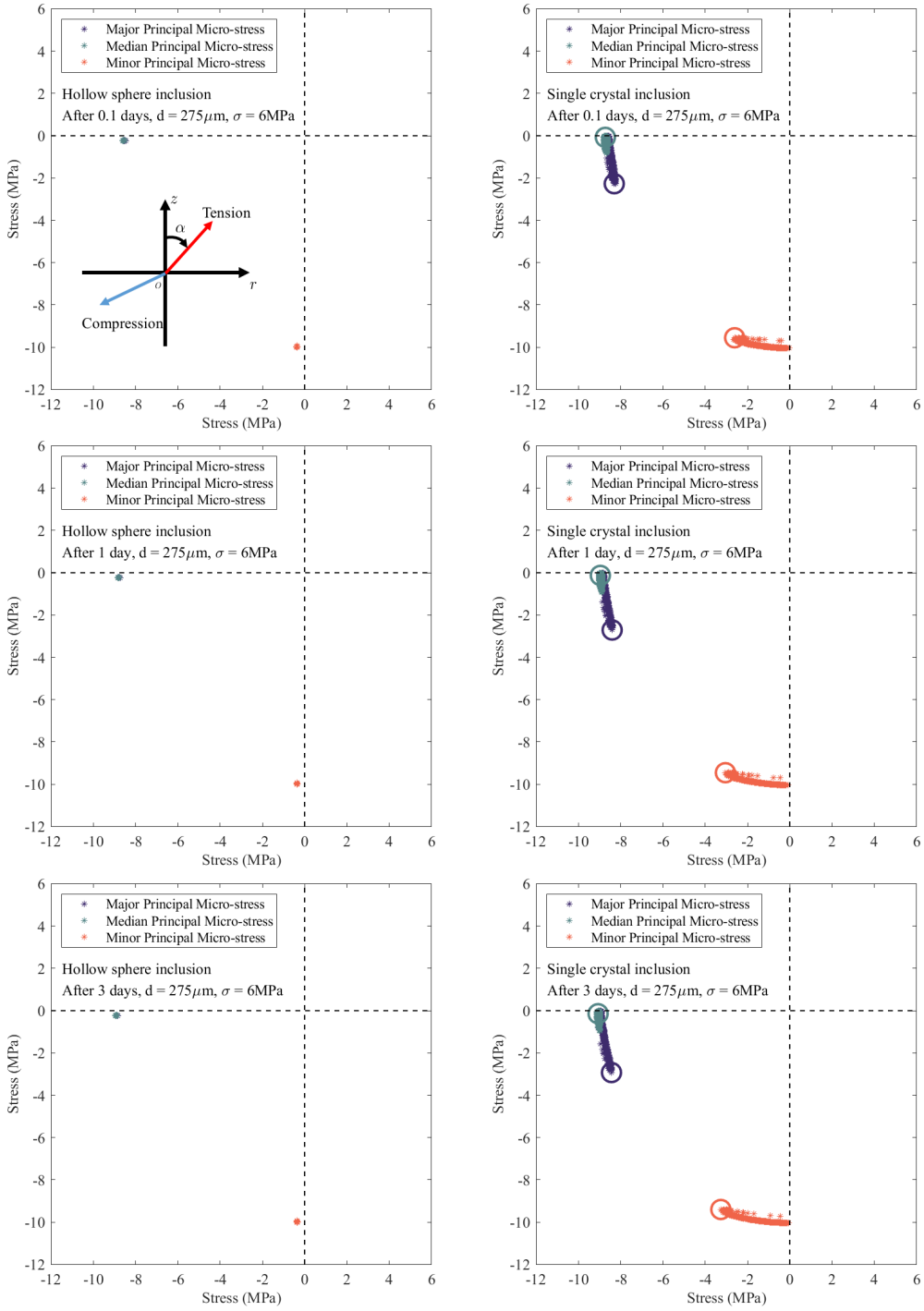

Figure 3: Microstress distributions in dry specimens subjected to an oedometric creep test under an axial stress of 6 MPa.

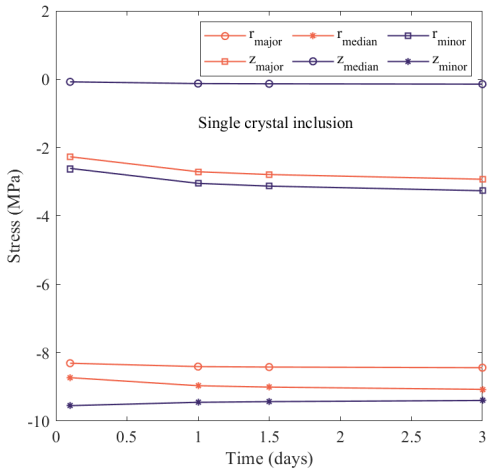

Figure 4: Evolution of principal stresses of one of the 500 crystal inclusions during the dry creep test under 6 MPa.

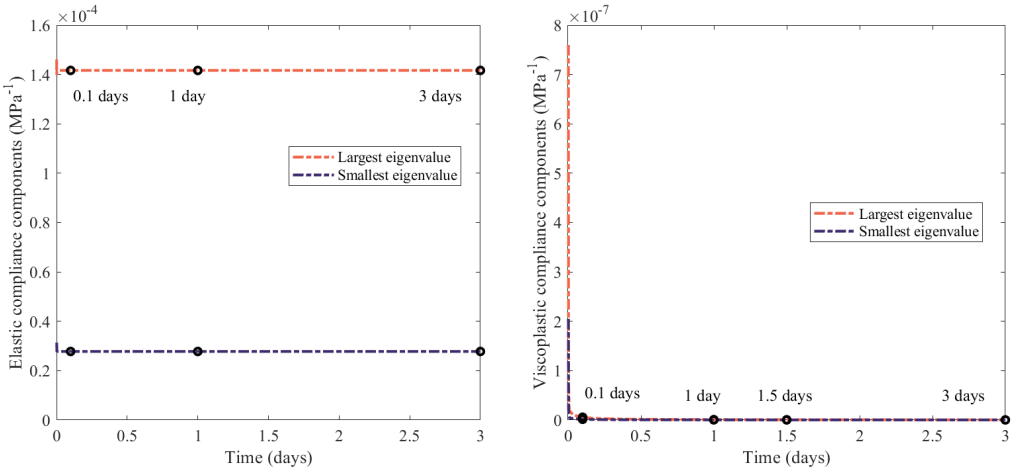

Figure 5: Evolution of the smallest and largest eigenvalues of the elastic compliance tensor (left) and viscoplastic compliance tensor (right) during the dry creep test under 6 MPa.

tion of the pores inside the hollow sphere inclusions was set equal to the initial porosity of the specimen under study. A lognormal distribution was assumed for the hollow sphere void radii, with a variance of 0.0001 mm^2 (Arson and Pereira, 2013). We used the dislocation parameters reported in Table 1 and we calibrated the pressure solution parameters against the curve of volumetric strain vs. time (Spiers et al., 1988) obtained under a stress of 1.05 MPa. Experimental data obtained under 0.53 MPa and 2.1 MPa were used for verification. All the experiments were performed on specimens with a grain size of $d = 196\mu m$. The calibrated pressure solution parameters are listed in Table 1 and Fig. 6 shows the comparison between experimental data and numerical results. The model predicts the high deformation rate that occurs in the first hours of the creep tests, and captures the increase of the deformation rate with the applied stress.

Fig. 7 shows the microscopic principal stresses in the different sets of inclusions for the wet specimen under an axial stress of 1.05 MPa. Fig. 8 shows the evolution of the principal microstresses in one of the 500 hollow sphere inclusions and in one of the 500 crystal inclusions. Due to the interaction between the different types of inclusions, the crystal inclusions undergo a larger deviatoric stress than in dry conditions, despite the lower axial stress applied during the experiment (see Fig. 4). The higher deviatoric stress yields a higher dislocation sliding rate. The changes of principal stress magnitude and direction slow down over time. Correspondingly, the evolution of compliance tensors becomes stable after 3 days (see Fig. 9). During active pressure solution, two competing processes occur. On the one hand, precipitation occurs in the voids of the hollow sphere inclusions, which increases the

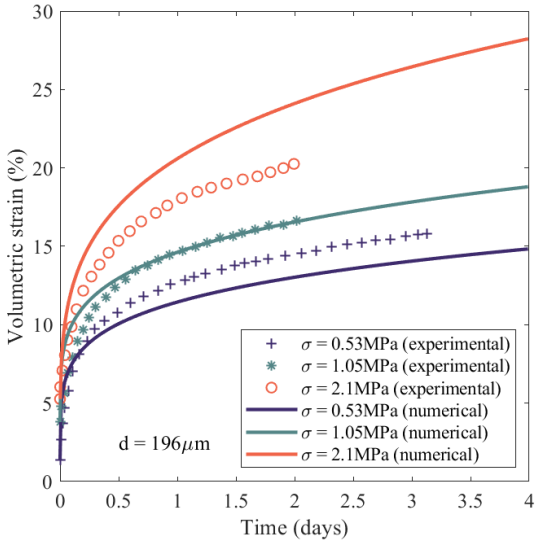

Figure 6: Comparison between numerical results and experimental data in wet conditions at various axial stresses.

elastic stiffness components. On the other hand, the length of the diffusion paths between the dissolution and precipitation sites increases as the voids get sealed over time, which decreases the pressure solution rate, and thus, the viscoplastic compliance tensor. The two-day volumetric deformation is predicted with an error that ranges between 15% and 20%, which may be due to the assumption that was made on the coefficient $Z = DCS$ that defines grain boundary diffusivity in Eq. 42. In this study, Z was considered constant, but it is potentially dependent on temperature and applied stress or strain (Spiers et al., 1990; Rutter, 1983).

The stark creep rate difference between dry and wet conditions is properly reproduced by the model. In the absence of further experimental data on the initial fabric of the salt specimens, we use the calibrated constitutive

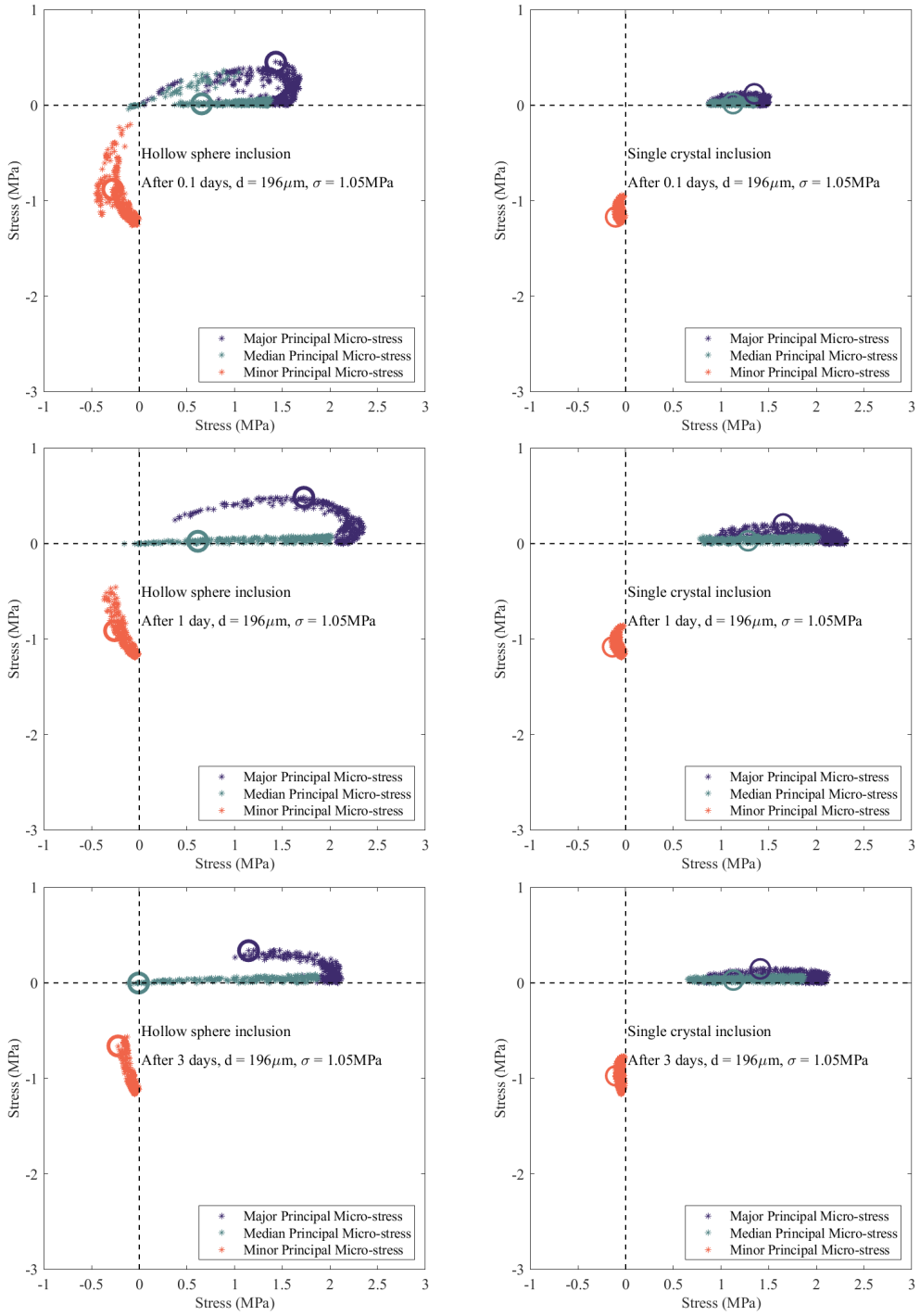

Figure 7: Microstress distributions in wet specimens subjected to an oedometric creep test under an axial stress of 1.05 MPa.

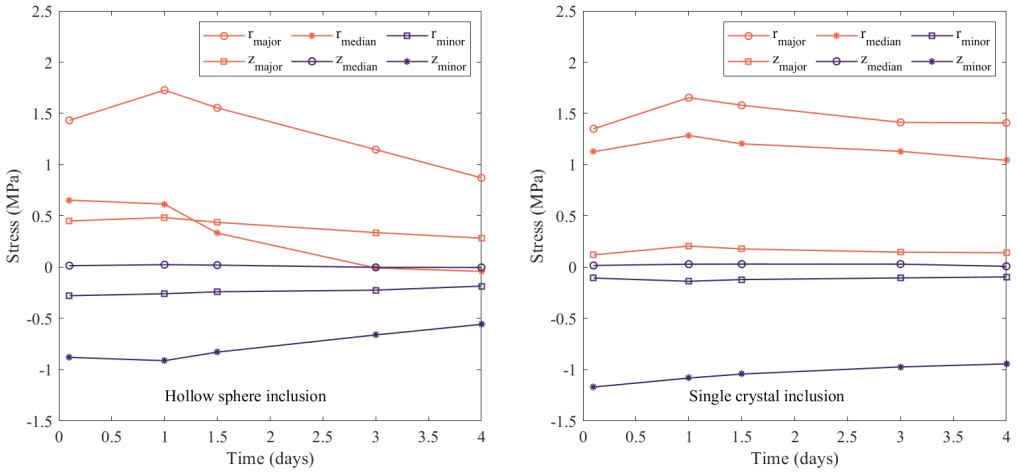

(a) Hollow sphere inclusion (b) Single crystal inclusion

Figure 8: Evolution of principal stresses of two example inclusions during the wet creep test under 1.05 MPa.

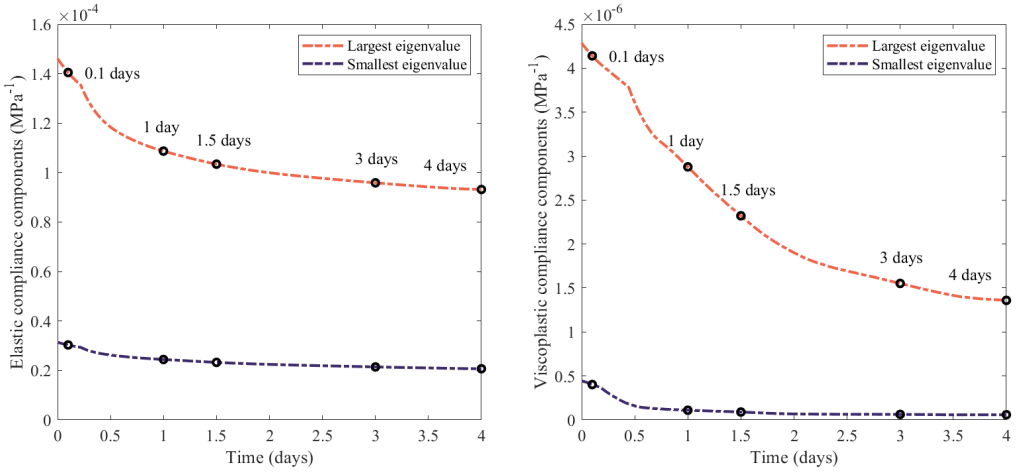

Figure 9: Evolution of the smallest and largest eigenvalues of the elastic compliance tensor (left) and viscoplastic compliance tensor (right) during the wet creep test under 1.05 MPa.

parameters reported in Table 1 to analyze the sensitivity of the model to stress, brine content, grain size and grain breakage.

5.3. Sensitivity to applied stress

Fig. 10 shows the distributions of microstresses in the wet specimens after 1 day for each applied stress simulated in Subsection 5.2. The higher the applied stress, the wider the microstresses distribution. That observation is true for both types of inclusion. Fig. 11 shows the variation of the eigenvalues of the elastic and viscoplastic compliance tensors with the axial stress. The increase of the major compliance eigenvalues with the applied stress explains the increase of deformation rate with the axial stress. At the microscopic level, the increase of deformation rate with applied stress can be explained by the dependence of pressure solution creep on compressive stress (see Eq. 47), and by the interaction between pressure solution and dislocation mechanisms, which increases the deviatoric stress and deformation rate of the single crystal inclusions.

5.4. Sensitivity to brine content

Results from Subsections 5.1 and 5.2 highlight the importance of the coupling between dislocation and pressure solution in wet conditions. In the following, we analyze the sensitivity of the behavior of the polycrystal to the brine content, through the parameter f_{HS}.

Fig. 12 shows the compaction creep curves obtained after simulating an oedometric compression test under 2.1 MPa with the model parameters reported in Table 1, for various brine contents (for $f_{\mathrm{HS}} = 0$; 0.25; 0.5; 0.75; 1). The reduction of brine content leads to a decrease of the strain rate. It

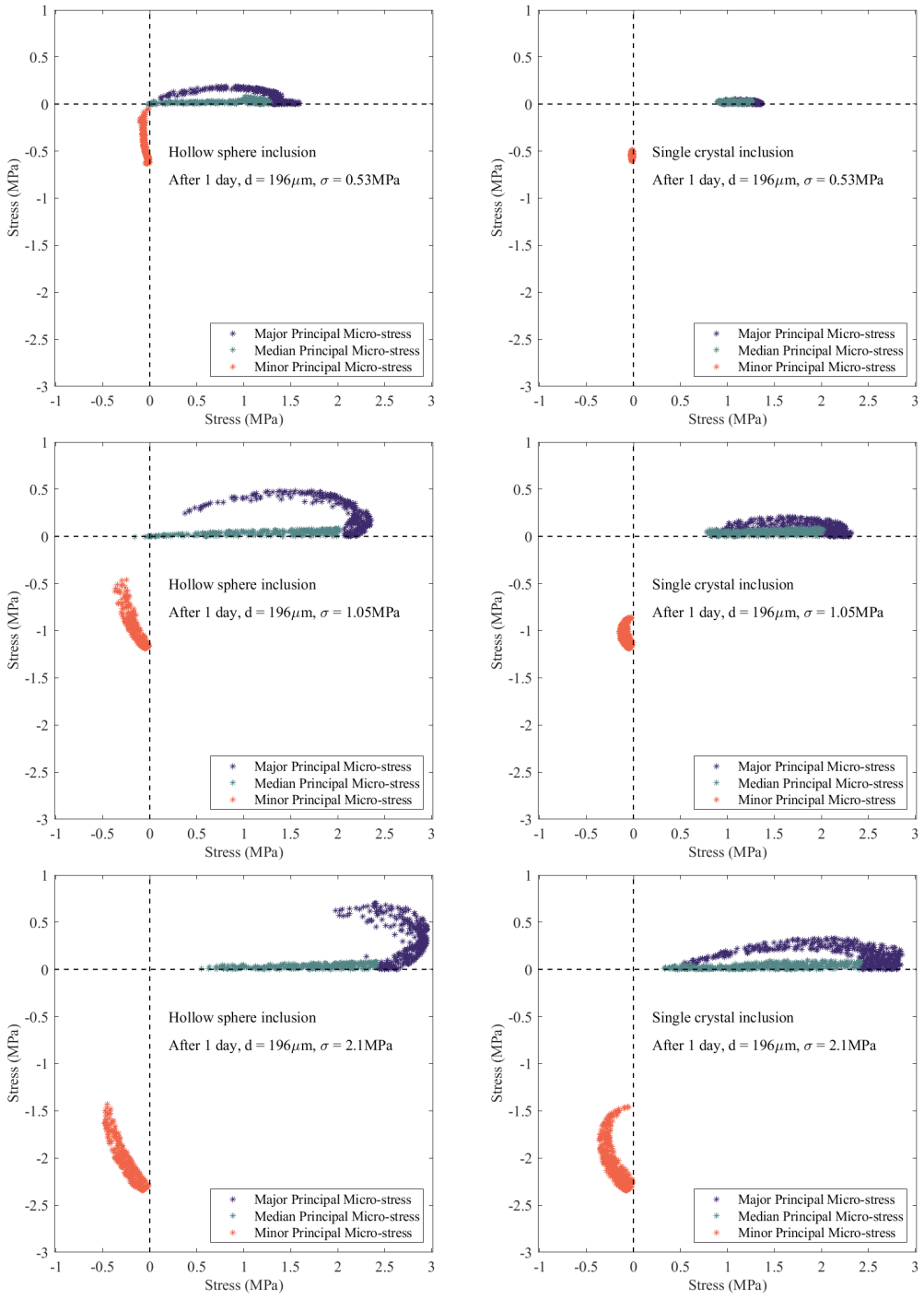

Figure 10: Microstress distributions in wet specimens after 1 day of oedometric creep test at various axial stresses.

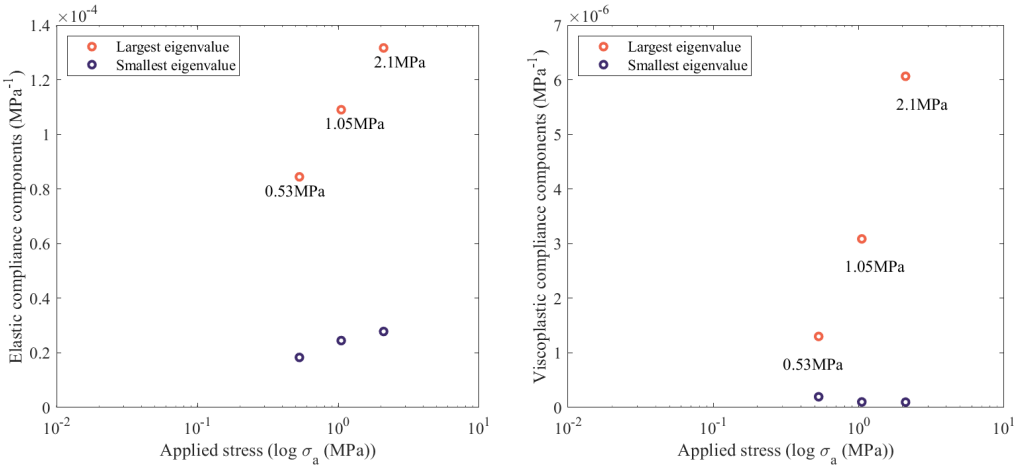

Figure 11: Comparison of the smallest and largest eigenvalues of the elastic compliance tensor (left) and viscoplastic compliance tensor (right) at various axial stresses, in wet conditions, after 1 day.

is noted that this reduction in deformation rate becomes significant when $f_{\mathrm{HS}} < 25\%$, which is consistent with the results reported by Spiers et al. (1988). The dependence of the deformation rate on brine content can be explained by the variations of the eigenvalues of the elastic and viscoplastic compliance tensors, shown in Fig. 13.

The microstress distributions are plotted in Fig. 14. It is evident that dislocation is the only viscoplastic deformation mechanism for the dry sample and therefore the densification rate is low. As the hollow sphere void volume fraction increases, the pressure solution creep rate increases and the microstress fields are redistributed such that crystal inclusions sustain more tensile stress, which results in a larger dislocation creep rate.

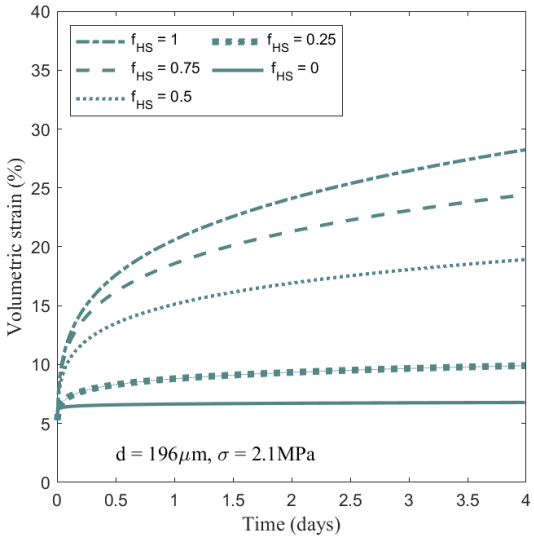

Figure 12: Creep curves obtained by simulating oedometric creep tests under 2.1 MPa with different brine contents.

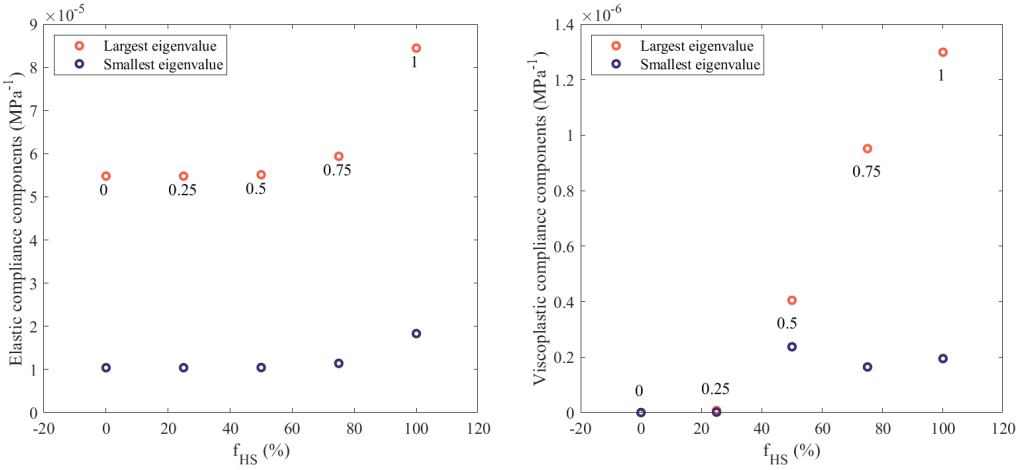

Figure 13: Comparison of the smallest and largest eigenvalues of the elastic compliance tensor (left) and viscoplastic compliance tensor (right) of wet specimens subjected to an oedometric creep test under 2.1 MPa, for different brine contents, after 1 day.

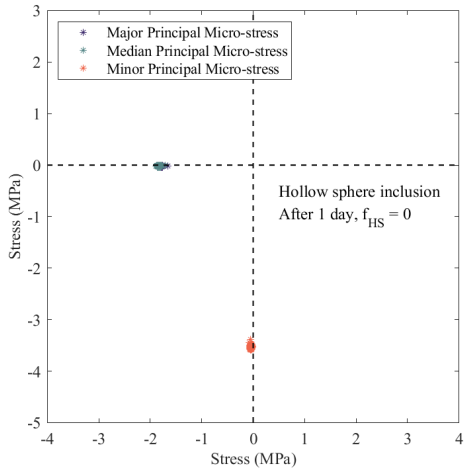
Major Principal Micro-stress
Median Principal Micro-stress
Minor Principal Micro-stress
Hollow sphere inclusion
After 1 day, f_{HS} = 0
Stress (MPa)
Stress (MPa)

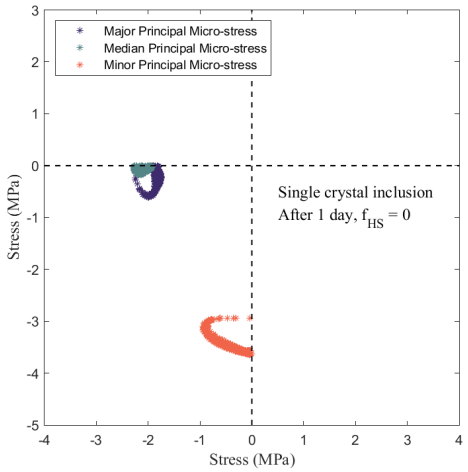
Major Principal Micro-stress
Median Principal Micro-stress
Minor Principal Micro-stress
Single crystal inclusion
After 1 day, f_{HS} = 0
Stress (MPa)
Stress (MPa)

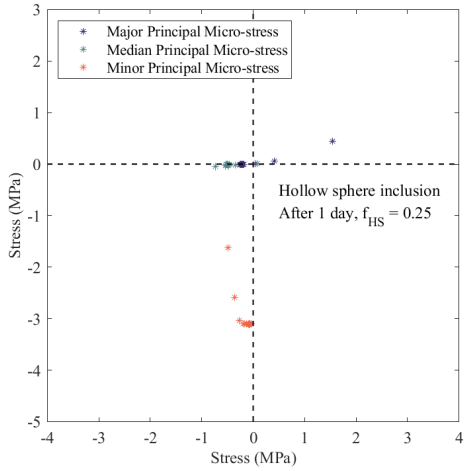
Major Principal Micro-stress
Median Principal Micro-stress
Minor Principal Micro-stress
Hollow sphere inclusion
After 1 day, f_{HS} = 0.25
Stress (MPa)
Stress (MPa)

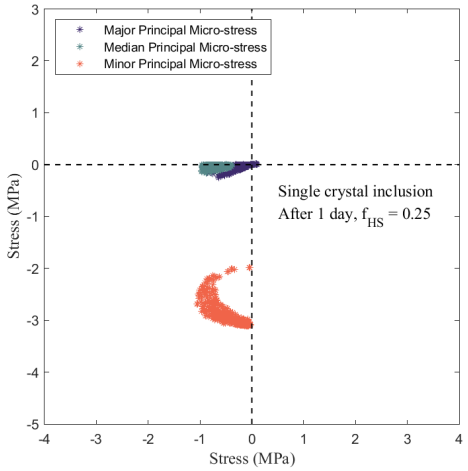
Major Principal Micro-stress
Median Principal Micro-stress
Minor Principal Micro-stress
Single crystal inclusion
After 1 day, f_{HS} = 0.25
Stress (MPa)
Stress (MPa)

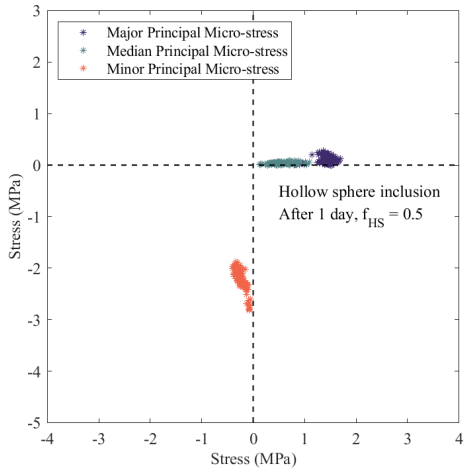
Major Principal Micro-stress
Median Principal Micro-stress
Minor Principal Micro-stress
Hollow sphere inclusion
After 1 day, f_{HS} = 0.5
Stress (MPa)
Stress (MPa)

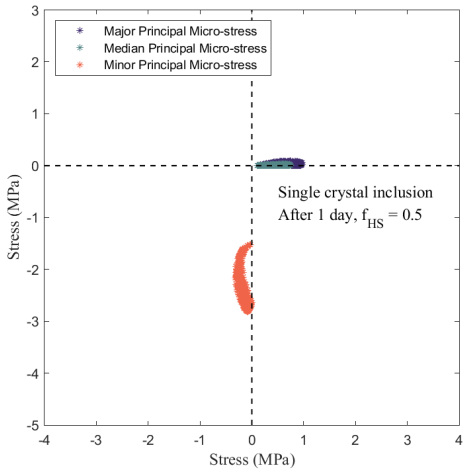
Major Principal Micro-stress
Median Principal Micro-stress
Minor Principal Micro-stress
Single crystal inclusion
After 1 day, f_{HS} = 0.5
Stress (MPa)
Stress (MPa)

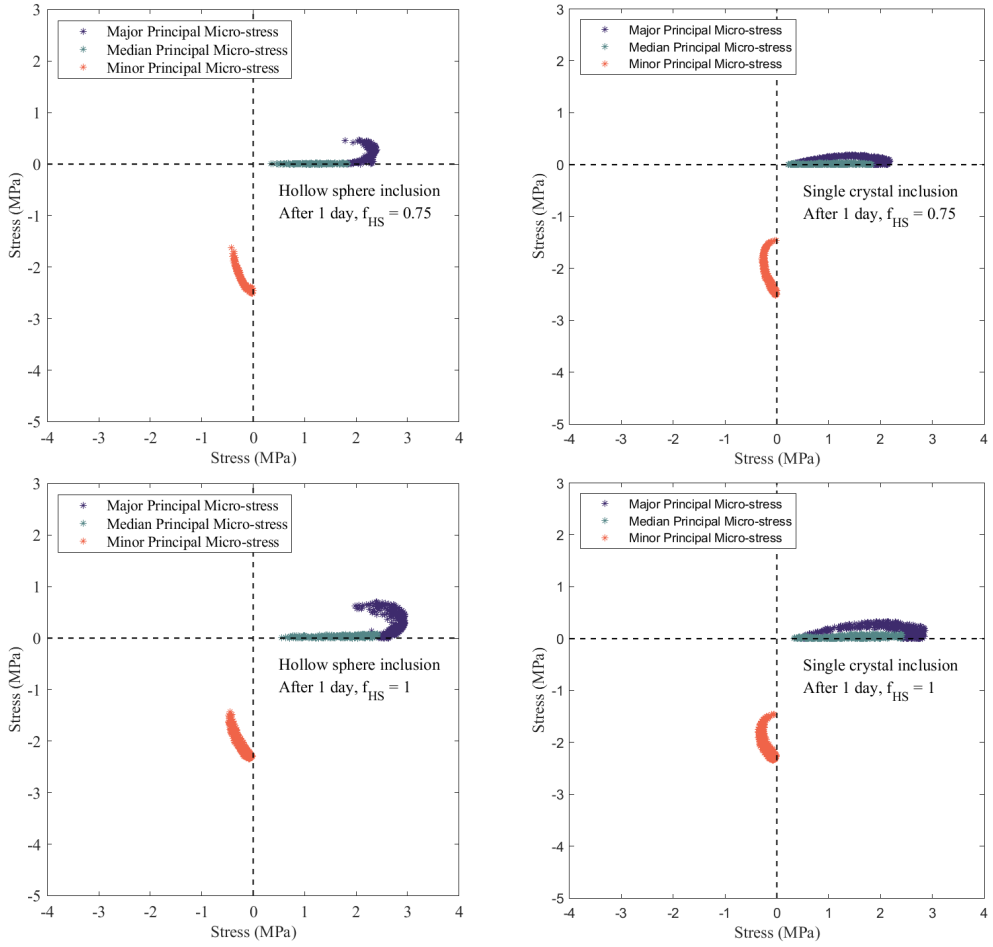

Figure 14: Microstress distributions in specimens of various brine contents, after 1 day of oedometric creep test under 2.1 MPa.

5.5. Sensitivity to grain size and strength

In the following, we analyze the sensitivity of the model to grain size by simulating the wet creep test under an axial stress of 2.1 MPa, with the model parameters reported in Table 1. The grain size is controlled by parameter A in Eq. 42. Fig. 15 shows that the model predictions reproduce the trends observed experimentally (Spiers et al., 1988). The microstress distributions calculated after 1 day are plotted in Fig. 16. It is interesting to note that the major and minor principal stresses get more widely distributed as the grain size within the hollow sphere inclusions is decreased. Fig. 17 shows the corresponding compliance tensors. It is clear that at constant axial stress, both elastic and viscoplastic compliance tensors exhibit a dependence on grain size. This observation can be explained by Eq. 47: the pressure solution deformation rate is essentially controlled by the grain size. The larger the grain size, the less contact surfaces in the REV and the longer the diffusion paths, which results in a smaller deformation rate in the hollow sphere inclusions and, due to the coupled inteaction laws, in a smaller deviatoric stress in the crystal inclusions. At the REV scale, we observe that the deformation rate increases when the grain size decreases.

We now introduce a grain breakage mechanism in the model, by which the dislocating crystal inclusions are progressively transformed into fluid-filled pore heterogeneities. This phase transformation allows representation of weakening and mechanical damage at REV scale. Following Pouya et al. (2016), we assume that a crystal breaks when the major principal local stress exceeds the tensile strength of the salt mono-crystal (i.e., 2MPa). An oedometric compression test under 1.05 MPa is simulated with account for grain

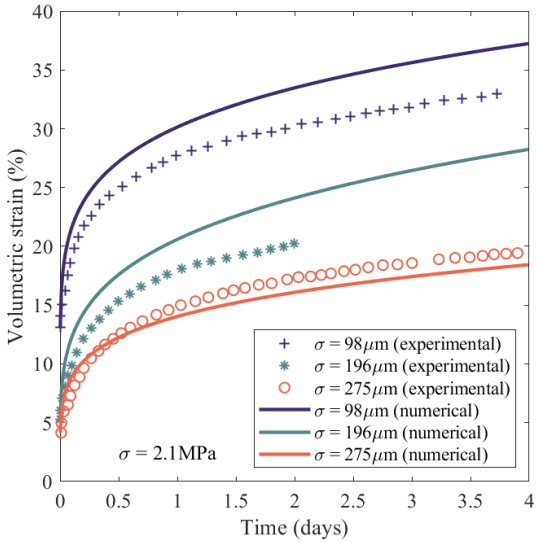

Figure 15: Comparison between numerical results and experimental data for a wet creep test under 2.1 MPa, for different grain sizes.

breakage with the model parameters reported in Table 1. Grain breakage is observed after 0.275 days (see Figs. 18 and 19), because the high deformation rate of the hollow sphere inclusions accelerates the concentration of tensile stress in the crystal inclusions. The abrupt increase of volumetric strain rate noted in Fig. 18 indicates that the model can capture the acceleration of the creep rate, sometimes called tertiary creep, often observed in experiments (Fuenkajorn and Phueakphum, 2010). Since the Eshelby tensor involved in the interaction laws depends on the volume fraction of the fluid-filled pore inclusions, it is possible to calculate the increase of compliance due to grain breakage, as shown in Fig. 20.

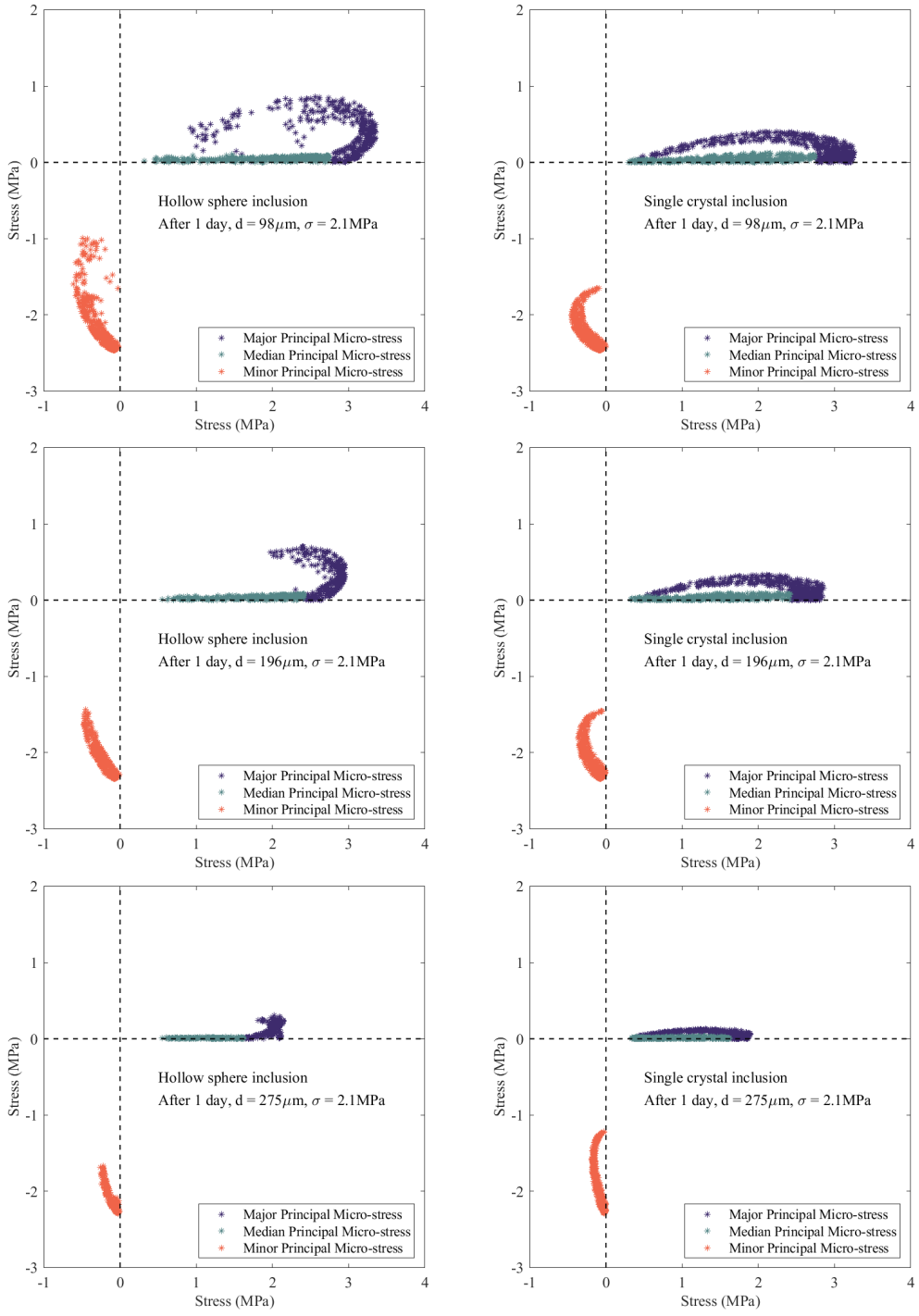

Figure 16: Microstress distributions in wet specimens after 1 day of oedometric creep test under 2.1 MPa, for different grain sizes.

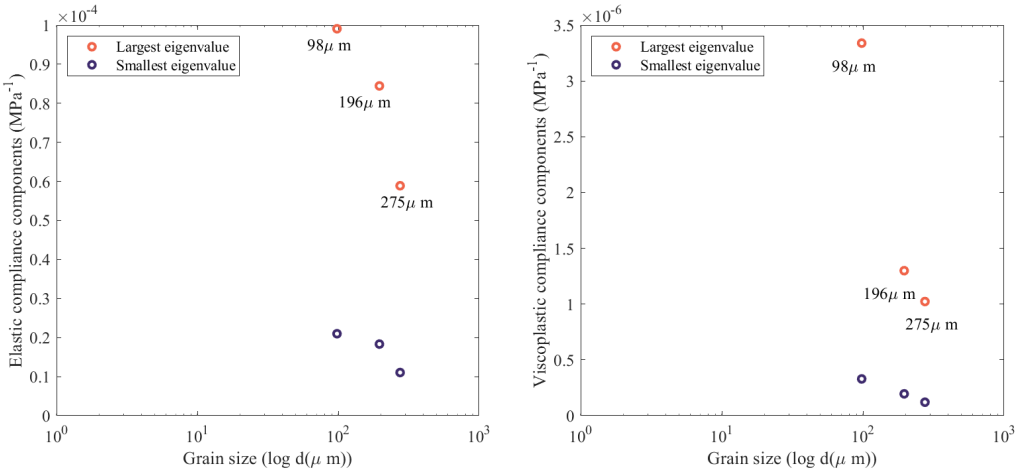

Figure 17: Comparison of the smallest and largest eigenvalues of the elastic compliance tensor (left) and viscoplastic compliance tensor (right) of wet specimens subjected to an oedometric creep test under 2.1 MPa, for different grain sizes, after 1 day.

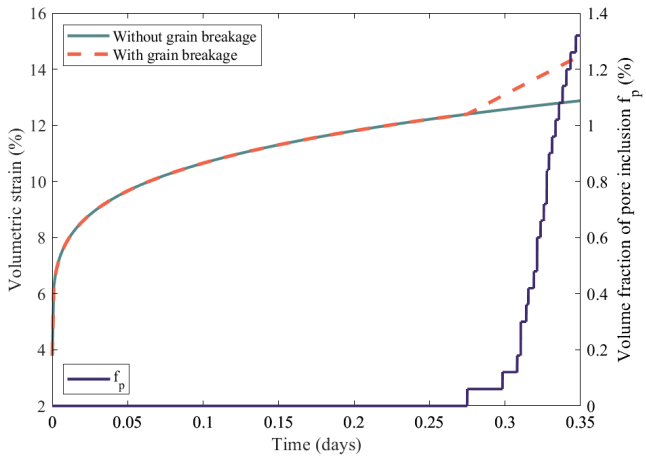

Figure 18: Evolution of volumetric strain and volume fraction of pore inclusions during an oedometric creep test under 1.05 MPa with account for grain breakage.

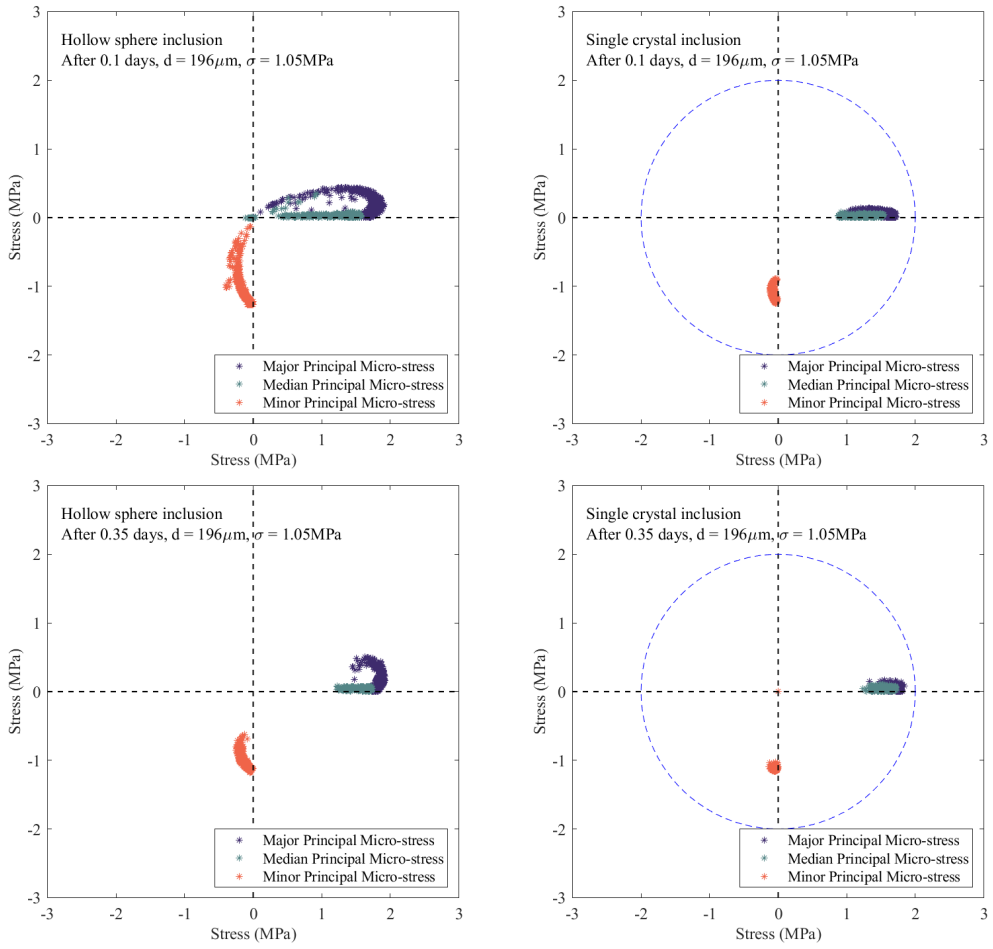

Figure 19: Microstress distributions in wet specimens subjected to an oedometric creep test under a compression stress of 1.05 MPa, with account for grain breakage.

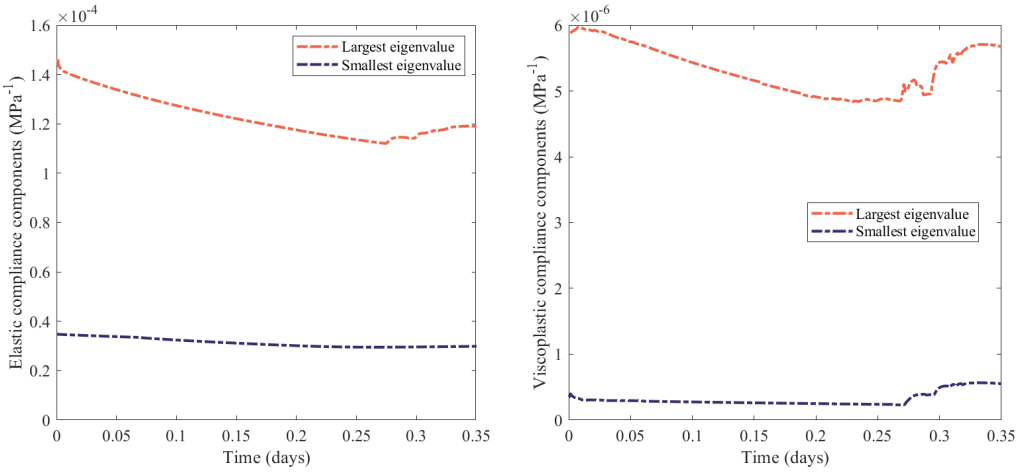

Figure 20: Evolution of the smallest and largest eigenvalues of the elastic compliance tensor (left) and viscoplastic compliance tensor (right) during a wet creep test under 1.05 MPa, with account for grain breakage.

6. Conclusions

This paper presents a self-consistent method to predict the elastic-viscoplastic behavior of porous polycrystals subjected to dislocation glide and pressure solution. The HEM is composed of three phases: single-crystal inclusions that are subject to dislocation, hollow sphere inclusions that are subject to pressure solution, and isolated fluid-filled pore inclusions. The model acounts for the transformation of sliding crystals to pores by grain breakage. Additionally, important contributions of the proposed work are the coupling between two non-linear time-dependent deformation mechanisms and the rigorous estimate of elastic and viscoplastic macroscopic stiffness and compliance tensors. The microscopic and macroscopic constitutive relationships are approximated by affine models. A tangent linearization prevents the overly stiff response that would be obtained at macro-scale with secant compliance

tensors. No specific form of anisotropy is assumed, and the formulation is generalizable to any type of polycrystal in which two time-dependent mechanisms occur under the same conditions of stress, humidity and temperature. To the authors' best knowledge, the couplings and the competition between dislocation and pressure solution had never been analyzed through the lens of micromechanics. We provide the details of the iterative algorithm that was implemented to solve the nested inclusion/matrix interaction problems, and we propose a staggered calibration procedure, taking halite as a model material for the sake of illustration.

The results obtained have significant implications, particularly in geomechanics. For instance, it is well known that in salt rock, dislocation glide favors crack propagation, while pressure solution induces crack "healing" and recovery of stiffness and strength. The results obtained in this paper confirm that pressure solution leads to a decrease of both elastic and viscoplastic compliance components if grain breakage is ignored. Otherwise, pressure solution increases the deviatoric stress in solid crystals, which results in larger deformation rates, grain breakage and an abrupt increase of elastic and viscoplastic compliance components. Higher stress and/or higher brine content enhance the coupled effects of pressure solution and dislocation. At the microscopic scale, pressure solution is controlled by stress and grain size: the higher the stress and the smaller the grains, the higher pressure solution deformation rate. Pressure solution alone is self-limited, because in-pore precipitation hinders the diffusion of ions from dissolution sites to precipitation sites. These trends are properly captured by the model. In salt rock, dislocation and pressure solution occur simultaneously under typical

stress and temperature geostorage conditions. Therefore, a micromechanical understanding of the time-evolution of halite deformation rate and macroscopic properties is critical to the safety of geological storage facilities. The model can be used to design halite microstructures that are favorable to waste or energy containment. For instance, simulation results show that pressure solution is delayed by the occurrence of larger grains and by the entrapment of fluid in isolated pores as opposed to intergranular films. An interesting feature of the model is the representation of the pore space, which allows distinguishing the deformation mechanisms of these isolated pores from those of the pores where precipitation occurs.

A natural extension of the present work is the prediction of progressive mechanical damage in the inclusions and in the HEM. Damage initiation and propagation criteria can be incorporated in the constitutive relationships at the microscopic scale, and could complement the current model of phase change from crystal to pore. Another possible improvement of the model is the extension of the constitutive framework from the first-order estimates provided by the affine formulation to higher-order estimates, which could represent the high deformation gradients that may exist inside single crystals and at the vicinity of the pores. Considering field fluctuations within each phase via high-order statistical moments is a natural next step in the proposed modeling efforts.

Acknowledgments

This research was funded by the U.S. National Science Foundation, under grant CMMI 1552368: "CAREER: Multiphysics Damage and Healing of

Rocks for Performance Enhancement of Geo-Storage Systems - A Bottom-Up Research and Education Approach".

Appendix A. Finite Eshelby' solution

Using the finite Mori-Tanaka method, the homogenized elastic coefficients of the hollow sphere inclusion are the following:

$$\begin{aligned} \overline{K}^e &= K^s - \phi K^s [1 - (1-\phi)\Delta s_1^F]^{-1} \\ \overline{\mu}^e &= \mu^s - \phi \mu^s [1 - (1-\phi)\Delta s_2^F]^{-1} \\ \mathbb{A}^p &= [\mathbb{I} - (1-\phi)(< \mathbb{S}^{I,F} > - < \mathbb{S}^{E,F} >)]^{-1} \end{aligned} \tag{A.1}$$

where $\overline{K}^e$ and $\overline{\mu}^e$ denote the effective bulk elastic modulus and shear elastic modulus, respectively. The coefficients $\Delta s_i^F = s_i^{I,F} - s_i^{E,F}$ for $i = 1, 2$ can be expressed as:

$$\begin{aligned} \Delta s_1^\infty &= \frac{1+\nu^s}{3(1-\nu^s)} \\ \Delta s_1^D &= \Delta s_1^N = \Delta s_1^\infty \\ \Delta s_2^\infty &= \frac{2(4-5\nu^s)}{15(1-\nu^s)} \\ \Delta s_2^D &= \Delta s_2^\infty - 21\gamma_u \frac{1-\phi^{2/3}}{1-\phi} \\ \Delta s_2^F &= \Delta s_2^\infty + 21\gamma_t \frac{1-\phi^{2/3}}{1-\phi} \end{aligned} \tag{A.2}$$

in which ∞ denotes the original infinite Eshelby tensor. The coefficients γ_u and γ_t are written as:

$$\begin{aligned} \gamma_u &= \frac{\phi(1-\phi^{2/3})}{10(1-\nu)(7-10\nu)} \\ \gamma_t &= \frac{4\phi(1-\phi^{2/3})}{10(1-\nu)(7+5\nu)} \end{aligned} \tag{A.3}$$

References

Adams, B.L., Olson, T., 1998. The mesostructure—properties linkage in polycrystals. Progress in Materials Science 43, 1–87.

Agoras, M., Avazmohammadi, R., Castañeda, P.P., 2016. Incremental variational procedure for elasto-viscoplastic composites and application to polymer-and metal-matrix composites reinforced by spheroidal elastic particles. International Journal of Solids and Structures 97, 668–686.

Arson, C., 2020. Micro-macro mechanics of damage and healing in rocks. Open Geomechanics 2, 1–41.

Arson, C., Pereira, J.M., 2013. Influence of damage on pore size distribution and permeability of rocks. International Journal for Numerical and Analytical Methods in Geomechanics 37, 810–831.

Arson, C., Xu, H., Chester, F.M., 2012. On the definition of damage in time-dependent healing models for salt rock. Géotechnique letters 2, 67–71.

Asaro, R.J., 1983. Crystal plasticity .

Ashby, M.F., 1972. A first report on deformation-mechanism maps. Acta Metallurgica 20, 887–897.

Berveiller, M., Zaoui, A., 1979. An extension of the self-consistent scheme to plastically-flowing polycrystals. Journal of the Mechanics and Physics of Solids 26, 325–344.

Brassart, L., Stainier, L., Doghri, I., Delannay, L., 2012. Homogenization of elasto-(visco) plastic composites based on an incremental variational principle. International Journal of Plasticity 36, 86–112.

Budiansky, B., Wu, T.T., 1962. Theoretical prediction of plastic strains of polycrystals. Proc. 4th US Cong. Appl. Mech. 1175.

Carter, N., Horseman, S., Russell, J., Handin, J., 1993. Rheology of rocksalt. Journal of Structural Geology 15, 1257–1271.

Carter, N.L., Hansen, F.D., Senseny, P.E., 1982. Stress magnitudes in natural rock salt. Journal of Geophysical Research: Solid Earth 87, 9289–9300.

Castañeda, P.P., 1991. The effective mechanical properties of nonlinear isotropic composites. Journal of the Mechanics and Physics of Solids 39, 45–71.

Castañeda, P.P., 2002a. Second-order homogenization estimates for nonlinear composites incorporating field fluctuations: I—theory. Journal of the Mechanics and Physics of Solids 50, 737–757.

Castañeda, P.P., 2002b. Second-order homogenization estimates for nonlinear composites incorporating field fluctuations: Ii—applications. Journal of the Mechanics and Physics of Solids 50, 759–782.

Chan, K.S., Bodner, S., Munson, D., Fossum, A., 1996. A constitutive model for representing coupled creep, fracture, and healing in rock salt. Technical Report. Sandia National Labs., Albuquerque, NM (United States).

Clyne, T., Withers, P., 1995. An introduction to metal matrix composites. Cambridge university press.

Doghri, I., Adam, L., Bilger, N., 2010. Mean-field homogenization of elasto-viscoplastic composites based on a general incrementally affine linearization method. International Journal of Plasticity 26, 219–238.

Dormieux, L., Kondo, D., Ulm, F.J., 2006. Microporomechanics. John Wiley & Sons.

Eshelby, J.D., 1957. The determination of the elastic field of an ellipsoidal inclusion, and related problems. Proc. R. Soc. Lond. A 241, 376–396.

Fan, J., Jiang, D., Liu, W., Wu, F., Chen, J., Daemen, J., 2019. Discontinuous fatigue of salt rock with low-stress intervals. International Journal of Rock Mechanics and Mining Sciences 115, 77–86.

Fuenkajorn, K., Phueakphum, D., 2010. Effects of cyclic loading on mechanical properties of maha sarakham salt. Engineering Geology 112, 43–52.

Gavazzi, A., Lagoudas, D., 1990. On the numerical evaluation of eshelby's tensor and its application to elastoplastic fibrous composites. Computational mechanics 7, 13–19.

González, C., LLorca, J., 2000. A self-consistent approach to the elasto-plastic behaviour of two-phase materials including damage. Journal of the Mechanics and Physics of Solids 48, 675–692.

Gundersen, E., Renard, F., Dysthe, D.K., Bjørlykke, K., Jamtveit, B., 2002.

Coupling between pressure solution creep and diffusive mass transport in porous rocks. Journal of Geophysical Research: Solid Earth 107, ECV–19.

Hill, R., 1965. Continuum micro-mechanics of elastoplastic polycrystals. Journal of the Mechanics and Physics of Solids 13, 89–101.

Hunsche, U., Hampel, A., 1999. Rock salt—the mechanical properties of the host rock material for a radioactive waste repository. Engineering geology 52, 271–291.

Hutchinson, J., 1970. Elastic-plastic behaviour of polycrystalline metals and composites. Proceedings of the Royal Society of London. A. Mathematical and Physical Sciences 319, 247–272.

Hutchinson, J.W., 1976. Bounds and self-consistent estimates for creep of polycrystalline materials. Proc. R. Soc. Lond. A 348, 101–127.

Iwakuma, T., Nemat-Nasser, S., 1984. Finite elastic-plastic deformation of polycrystalline metals. Proceedings of the Royal Society of London. A. Mathematical and Physical Sciences 394, 87–119.

Jeong, Y., Tomé, C.N., 2019. Extension of the visco-plastic self-consistent model to account for elasto-visco-plastic behavior using a perturbed visco-plastic approach. Modelling and Simulation in Materials Science and Engineering 27, 085013.

Jiang, D., 2007. Numerical modeling of the motion of rigid ellipsoidal objects in slow viscous flows: a new approach. Journal of Structural Geology 29, 189–200.

Ju, J., 1991. On two-dimensinal self-consistent micromechanical damage models for brittle solids. International Journal of Solids and Structures 27, 227–258.

Kröner, E., 1958. Berechnung der elastischen konstanten des vielkristalls aus den konstanten des einkristalls. Zeitschrift für Physik 151, 504–518.

Kröner, E., 1961. Zur plastischen verformung des vielkristalls. Acta metallurgica 9, 155–161.

Lahellec, N., Suquet, P., 2007a. On the effective behavior of nonlinear inelastic composites: I. incremental variational principles. Journal of the Mechanics and Physics of Solids 55, 1932–1963.

Lahellec, N., Suquet, P., 2007b. On the effective behavior of nonlinear inelastic composites: Ii: A second-order procedure. Journal of the Mechanics and Physics of Solids 55, 1964–1992.

Lahellec, N., Suquet, P., 2013. Effective response and field statistics in elasto-plastic and elasto-viscoplastic composites under radial and non-radial loadings. International Journal of Plasticity 42, 1–30.

Laws, N., McLaughlin, R., 1979. The effect of fibre length on the overall moduli of composite materials. Journal of the Mechanics and Physics of Solids 27, 1–13.

Lebensohn, R., Tomé, C., Maudlin, P., 2004. A selfconsistent formulation for the prediction of the anisotropic behavior of viscoplastic polycrystals with voids. Journal of the Mechanics and Physics of Solids 52, 249–278.

Lebensohn, R., Turner, P., Signorelli, J., Canova, G., Tomé, C., 1998. Calculation of intergranular stresses based on a large-strain viscoplastic self-consistent polycrystal model. Modelling and Simulation in Materials Science and Engineering 6, 447.

Lebensohn, R.A., 2001. N-site modeling of a 3d viscoplastic polycrystal using fast fourier transform. Acta materialia 49, 2723–2737.

Lebensohn, R.A., Brenner, R., Castelnau, O., Rollett, A.D., 2008. Orientation image-based micromechanical modelling of subgrain texture evolution in polycrystalline copper. Acta Materialia 56, 3914–3926.

Lebensohn, R.A., Kanjarla, A.K., Eisenlohr, P., 2012. An elasto-viscoplastic formulation based on fast fourier transforms for the prediction of micromechanical fields in polycrystalline materials. International Journal of Plasticity 32, 59–69.

Lebensohn, R.A., Tomé, C., 1993. A self-consistent anisotropic approach for the simulation of plastic deformation and texture development of polycrystals: application to zirconium alloys. Acta metallurgica et materialia 41, 2611–2624.

Lebensohn, R.A., Tomé, C.N., Maudlin, P.J., 2003. An Extended Self-Consistent Viscoplastic Polycrystal Formulation: Application to Polycrystals with Voids. Technical Report. Los Alamos National Lab.(LANL), Los Alamos, NM (United States).

Lehner, F.K., 1990. Thermodynamics of rock deformation by pressure solu-

tion, in: Deformation processes in minerals, ceramics and rocks. Springer, pp. 296–333.

Lehner, F.K., 1995. A model for intergranular pressure solution in open systems. Tectonophysics 245, 153–170.

Li, S., Sauer, R.A., Wang, G., 2007a. The eshelby tensors in a finite spherical domain—part i: theoretical formulations .

Li, S., Wang, G., Sauer, R.A., 2007b. The eshelby tensors in a finite spherical domain—part ii: applications to homogenization. Journal of Applied Mechanics 74, 784–797.

Masson, R., Bornert, M., Suquet, P., Zaoui, A., 2000. An affine formulation for the prediction of the effective properties of nonlinear composites and polycrystals. Journal of the Mechanics and Physics of Solids 48, 1203–1227.

Masson, R., Zaoui, A., 1999. Self-consistent estimates for the rate-dependent elastoplastic behaviour of polycrystalline materials. Journal of the Mechanics and Physics of Solids 47, 1543–1568.

Mercier, S., Molinari, A., 2009. Homogenization of elastic–viscoplastic heterogeneous materials: Self-consistent and mori-tanaka schemes. International Journal of Plasticity 25, 1024–1048.

Miao, S., Wang, M.L., Schreyer, H.L., 1995. Constitutive models for healing of materials with application to compaction of crushed rock salt. Journal of Engineering Mechanics 121, 1122–1129.

Michel, J., Moulinec, H., Suquet, P., 2000. A computational method based on augmented lagrangians and fast fourier transforms for composites with high contrast. CMES(Computer Modelling in Engineering & Sciences) 1, 79–88.

Molinari, A., 2002. Averaging models for heterogeneous viscoplastic and elastic viscoplastic materials. Journal of engineering materials and technology 124, 62–70.

Molinari, A., Ahzi, S., Kouddane, R., 1997. On the self-consistent modeling of elastic-plastic behavior of polycrystals. Mechanics of Materials 26, 43–62.

Molinari, A., Canova, G., Ahzi, S., 1987. A self consistent approach of the large deformation polycrystal viscoplasticity. Acta Metallurgica 35, 2983–2994.

Mori, T., Tanaka, K., 1973. Average stress in matrix and average elastic energy of materials with misfitting inclusions. Acta metallurgica 21, 571–574.

Moulinec, H., Suquet, P., 1994. A fast numerical method for computing the linear and nonlinear mechanical properties of composites. Comptes rendus de l'Académie des sciences. Série II. Mécanique, physique, chimie, astronomie. .

Moulinec, H., Suquet, P., 1998. A numerical method for computing the overall response of nonlinear composites with complex microstructure. Computer methods in applied mechanics and engineering 157, 69–94.

Munson, D., 1997. Constitutive model of creep in rock salt applied to underground room closure. International Journal of Rock Mechanics and Mining Sciences 34, 233–247.

Munson, D.E., Dawson, P., 1979. Constitutive model for the low temperature creep of salt (with application to WIPP). Technical Report. Sandia Labs.

Mura, T., 1987. Micromechanics of defects in solids. Martinus Nijhoff, Dordrecht.

Musienko, A., Tatschl, A., Schmidegg, K., Kolednik, O., Pippan, R., Cailletaud, G., 2007. Three-dimensional finite element simulation of a polycrystalline copper specimen. Acta materialia 55, 4121–4136.

Olivella, S., Gens, A., 2002. A constitutive model for crushed salt. International journal for numerical and analytical methods in geomechanics 26, 719–746.

Pluymakers, A.M., Spiers, C.J., 2015. Compaction creep of simulated anhydrite fault gouge by pressure solution: theory v. experiments and implications for fault sealing. Geological Society, London, Special Publications 409, 107–124.

Pouya, A., 2000. Micro-macro approach for the rock salt behaviour. European Journal of Mechanics - A/Solids 19, 1015 – 1028. doi:https://doi.org/10.1016/S0997-7538(00)00204-7.

Pouya, A., Zhu, C., Arson, C., 2016. Micro-macro approach of salt viscous fatigue under cyclic loading. Mechanics of Materials 93, 13–31.

Raj, R., Ashby, M., 1971. On grain boundary sliding and diffusional creep. Metallurgical transactions 2, 1113–1127.

Roedder, E., 1984. The fluids in salt. American Mineralogist 69, 413–439.

Roters, F., Eisenlohr, P., Hantcherli, L., Tjahjanto, D.D., Bieler, T.R., Raabe, D., 2010. Overview of constitutive laws, kinematics, homogenization and multiscale methods in crystal plasticity finite-element modeling: Theory, experiments, applications. Acta Materialia 58, 1152–1211.

Rovinelli, A., Proudhon, H., Lebensohn, R.A., Sangid, M.D., 2020. Assessing the reliability of fast fourier transform-based crystal plasticity simulations of a polycrystalline material near a crack tip. International Journal of Solids and Structures 184, 153–166.

Rutter, E., 1976. A discussion on natural strain and geological structure-the kinetics of rock deformation by pressure solution. Philosophical Transactions of the Royal Society of London. Series A, Mathematical and Physical Sciences 283, 203–219.

Rutter, E., 1983. Pressure solution in nature, theory and experiment. Journal of the Geological Society 140, 725–740.

Sauer, R., Wang, G., Li, S., 2008. The composite eshelby tensors and their applications to homogenization. Acta mechanica 197, 63–96.

Senseny, P., Hansen, F., Russell, J., Carter, N., Handin, J., 1992. Mechanical behaviour of rock salt: phenomenology and micromechanisms, in: International journal of rock mechanics and mining sciences & geomechanics abstracts, Elsevier. pp. 363–378.

Shen, X., Arson, C., 2019. An isotropic self-consistent homogenization scheme for chemo-mechanical healing driven by pressure solution in halite. International Journal of Solids and Structures 161, 96–110.

Shimizu, I., 1995. Kinetics of pressure solution creep in quartz: theoretical considerations. Tectonophysics 245, 121–134.

Spiers, C., Peach, C., Brzesowsky, R., Schutjens, P., Liezenberg, J., Zwart, H., 1988. Long-term rheological and transport properties of dry and wet salt rocks. Technical Report. Commission of the European Communities.

Spiers, C., Schutjens, P., Brzesowsky, R., Peach, C., Liezenberg, J., Zwart, H., 1990. Experimental determination of constitutive parameters governing creep of rocksalt by pressure solution. Geological Society, London, Special Publications 54, 215–227.

Spiers, C.J., Schutjens, P.M., 1990. Densification of crystalline aggregates by fluid-phase diffusional creep, in: Deformation processes in minerals, ceramics and rocks. Springer, pp. 334–353.

Staudtmeister, K., Rokahr, R., 1997. Rock mechanical design of storage caverns for natural gas in rock salt mass. International Journal of Rock Mechanics and Mining Sciences 34, 300–e1.

Ter Heege, J., De Bresser, J., Spiers, C., 2005. Dynamic recrystallization of wet synthetic polycrystalline halite: dependence of grain size distribution on flow stress, temperature and strain. Tectonophysics 396, 35–57.

Urai, J., Spiers, C., 2007. The effect of grain boundary water on deformation

mechanisms and rheology of rocksalt during long-term deformation, in: Proc. 6th Conf. Mech. Beh. of Salt, pp. 149–158.

Walpole, L., 1969. On the overall elastic moduli of composite materials. Journal of the Mechanics and Physics of Solids 17, 235–251.

Wang, H., Wu, P., Tomé, C., Wang, J., 2012. Study of lattice strains in magnesium alloy az31 based on a large strain elastic-viscoplastic self-consistent polycrystal model. International Journal of Solids and Structures 49, 2155–2167.

Watanabe, T., Peach, C.J., 2002. Electrical impedance measurement of plastically deforming halite rocks at 125 c and 50 mpa. Journal of Geophysical Research: Solid Earth 107, ECV–2.

Wawersik, W., Zeuch, D., 1986. Modeling and mechanistic interpretation of creep of rock salt below 200 c. Tectonophysics 121, 125–152.

Yasuhara, H., Elsworth, D., Polak, A., 2003. A mechanistic model for compaction of granular aggregates moderated by pressure solution. Journal of Geophysical Research: Solid Earth 108.

Zecevic, M., Lebensohn, R.A., 2020. New robust self-consistent homogenization schemes of elasto-viscoplastic polycrystals. International Journal of Solids and Structures .

Zhang, N., Shi, X., Wang, T., Yang, C., Liu, W., Ma, H., Daemen, J., 2017. Stability and availability evaluation of underground strategic petroleum reserve (spr) caverns in bedded rock salt of jintan, china. Energy 134, 504–514.